# The influence of grinding process on the mechanical behavior of SiC/SiC composite tubes under uniaxial tension

Claire Morel, E. Baranger, J. Lamon, C. Marques, S. Le Bras, J. Braun, C. Lorrette

*August, 2023*

# The influence of grinding process on the mechanical behavior of SiC/SiC composite tubes under uniaxial tension

C. Morel[a,b,c], E. Baranger[b], J. Lamon[b], C. Marques[a], S. Le Bras[a], J. Braun[d], C. Lorrette[a]

a : Université Paris-Saclay, CEA, Service de Recherches en Matériaux et procédés Avancés, 91191 Gif-sur-Yvette, France
b :Université Paris-Saclay, CentraleSupélec, ENS Paris-Saclay, CNRS, LMPS Laboratoire de Mécanique, 4 avenue des sciences, 91190 Gif-sur-Yvette, France
c :Université de Toulouse, Institut Clément Ader, CNRS UMR 5312, 3 Rue Caroline Aigle, 31400 Toulouse, France
d :CEA/DAM, Le Ripault, BP16, 37260 Monts, France

**Abstract**

SiC/SiC composites are candidates of interest for fuel cladding applications in pressurized light-water reactors. In this study, fuel cladding tubes were made by filament winding and the matrix was deposited by CVI (Chemical Vapour Infiltration), which results in surface irregularities and waviness defects. This paper examines the influence of grinding steps on the mechanical behavior of tube specimens. Different depths of inner and outer surface grinding are carried out from a reference grade. Cyclic tensile tests are then performed. Elastic behavior analysis shows that the machining of tubes does not cause pre-damage. Analysis of unload-reload cycles indicates that the internal slippage does not depend on the seal coat thickness and that the surface quality weakly influences damage in the loading direction. Damage in the shear plane and ultimate failure strength strongly depend on the inner seal coat thickness.

**Keywords** Ceramic-matrix composites (CMCs), Mechanical properties, Defects, Grinding process

# 1 Introduction

High-temperature strength and stability under irradiation of SiC/SiC composites could improve the safety of nuclear reactors, in particular in the framework of the EATF (Enhanced Accident Tolerant Fuel) application, which aims at higher safety margins for the fuel cladding in the event of loss of coolant accident (LOCA) [1, 2, 3]. Fuel cladding is the outer layer of the fuel pellets and is currently made of zirconium alloys in light water reactors. One envisaged solution is using SiC/SiC composite tubes to improve high-temperature resistance. Experimental campaigns have been realized on representative conditions of loss of coolant accidents such as pressure-sealed under oxygen and vapor at 1200 °C or under steam atmosphere at 1500 °C or critical heat flux test [4, 5, 6]. They have demonstrated the superior mechanical strength of cladding based on SiC/SiC over zirconium alloy cladding in those harsh conditions.

SiC/SiC composites for nuclear applications are generally reinforced by a Hi-Nicalon S (HNS) fibrous preform, manufactured by NGS Advances Co. [7]. The SiC matrix is introduced by Chemical Vapor Infiltration (CVI). The fibers and the matrix must be crystallized and as pure as possible SiC to avoid differential swelling of constituents due to irradiation. The CVI process leads to a high surface roughness of components. High roughness of the outer surfaces of tubes can introduce turbulence of coolant fluid inside the nuclear power plant. On the inner surface of cladding tubes, some hot spots could appear if the nominal distance between the fuel pellet and the cladding is not appropriate. Therefore, special attention is paid to the smoothing treatment of the inner and outer surfaces of the cladding. For the same purpose, Deck et al.[8] considered that surface roughness must be between 0.8 µm and 1.3 µm, ovality tolerance must be lower than ±25 µm and straightness must be lower than 0.25 mm over 300 mm tube length. As a result, two processes were studied by the authors to grind the inner and outer surfaces. For outer surfaces, end-feed centerless grinding was used [9]. This process allows the wearing of material from long tubes thanks to two rotating wheels. For SiC/SiC grinding, diamond wheels were used. For the inner surface, grinding was done thanks to three equally located cutting tools.

This article is focused on the mechanical behavior of SiC/SiC tubes. The macroscopic mechanical behavior of SiC/SiC tubes has been investigated for nuclear [10, 11, 12] but also for aeronautics applications, i.e., sublayer in turbine blade cooling systems or propulsion engine cooling system [13, 14]. However, the literature paid less attention to the influence of manufacturing on the mechanical behavior of SiC/SiC composite tubes.

Several studies have investigated the influence of grinding or machining processes at the microscopic scale on ceramic composites, essentially on C/C or C/SiC composites [15, 16]. Few studies focused on SiC/SiC materials with the exception of [17]. The machining process generates brittle fracture of the matrix and the fibers but also debonding at fiber/matrix interface [18]. These mechanisms can vary regarding the fiber orientation with respects to the cutting direction and the cutting conditions [15, 19, 20, 21]. The grinding process also generates fiber fracture, matrix cracking, or crush and debonding at fiber/matrix interface [22, 23]. Damage mechanisms can also vary depending on the fiber orientation with respect to the grinding direction, and parameters, and the shape of the grinding wheels [16, 24, 25, 26]. Therefore, CMC grinding and cutting processes induce locally the same defect family because the cutting mechanisms are identical, at shavings scale [27, Chapter 6].

The studies previously cited focused on the local defects induced by grinding or cutting. However, few studies focused on the influence of cutting or grinding at macroscopic length scale, with the exception of Neubrand et al. [28] for 2D-C/SiC composites cutting and Rösiger et al. [21] for 2D-C/C-SiC composites cutting. To the authors' knowledge, no studies focused on SiC/SiC tube grinding. This paper aims at determining the influence of grinding steps at the macroscopic length scale. In particular, the influence of surface roughness on macroscopic mechanical behavior has been investigated. Moreover, as the seal coat layers were

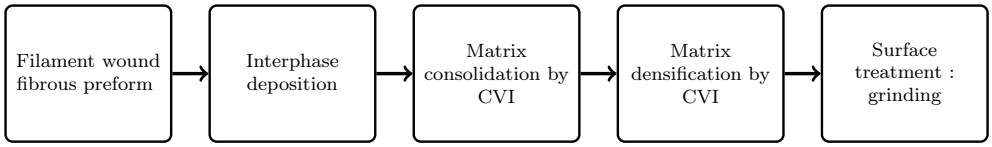


Figure 1: Description of the different manufacturing phases.

essentially removed during the grinding process, the influence of these layers, composed only of matrix, on the tube mechanical behavior has been investigated by performing tensile tests.

The tensile behavior of CMC exhibits several steps: elastic deformation, matrix cracking, and progressive breakage of fibers until the ultimate rupture [29, 30, 31, 32]. Damage modeling generally considers the load in the fiber direction and considers the fiber/matrix slip along the interphase cracks in the vicinity of matrix cracks [33, 34]. In the case of tubes with fibers inclined to the loading direction, the plies are subjected to multi-axial tension-shear loading. A return to compression during charge-discharge cycles allowed to separate the shear and tensile damage effects [35].

In this work, five grades of tubes were prepared, with various seal coat thicknesses and roughness on the inner and outer surfaces. The objective is to establish a rigorous method to analyze the results of uniaxial tensile tests on tubular specimens and to observe the influence of grinding steps.

# 2 Materials and method

## 2.1 Elaboration of SiC/SiC tubes by CVI process

The manufacturing process of CVI-SiC/SiC tubes consisted of five main steps (Figure 1). The four first steps were identical for the five grades studied in this article. Only the surface treatment was different.

First, the fibrous preform was made by filament winding on a cylindrical glass mandrel. Third-generation SiC fibers, Hi-Nicalon S, were used. They presented a high purity required for nuclear applications to avoid differential swelling under irradiation. They also endow the composite with a higher damage tolerance and mechanical strength compared to composite made from SiC Tyranno SA3 fibers [36]. The winding angle was fixed at $\pm 45°$ to obtain the same macroscopic behavior in axial tensile and internal pressure loading and to obtain high failure stress and strain. The winding parameters, including speed and fiber tension, were carefully chosen to avoid fiber rupture during manufacturing [7, 37].

Secondly, a pyrocarbon (PyC) of 30-100 nm thickness layer was deposited to allow the cracks deflection at fiber/matrix interphase.

Next, matrix was introduced by Chemical Vapour Infiltration in two phases. A first phase, named consolidation, allowed the infiltration of approximately 10 % of the matrix and consolidation of the fibrous preform. The removal of the cylindrical mandrel is then done at this stage. The second phase, named densification, allows to infiltrate the entire matrix and the obtained raw CVI tubes are considered as the reference tubes. The fiber content is approximately 29 %, the matrix 64 % and the porosity volumetric rate 7 %. The average roughness is 11 µm on the inner and 32 µm on the outer surfaces.

The last step consists of grinding the inner and outer surfaces to decrease the surface roughness to meet the dimensional specifications. End-feed centerless grinding is used on outer surfaces (Figure 2). This grinding process allows to abrade a cylindrical surface over a long distance. The grinding wheel in diamond allows the removal of material, whereas the second wheel, the regulating wheel, allows to guide the part and makes it go along the axis $\mathbf{e_z}$, tube axis of revolution. Both wheels turns in the same direction, with a slight inclination of the regulating wheel to drive the displacement of the part along the support. The speed of the grinding wheel is 1500 rpm, whereas the regulating wheel speed varies between 14 rpm and 20 rpm. The cutting depth is approximate 0.01 mm. The inner surface is removed thanks to three cutting tools equally distributed (Figure 3). The cutting force is distributed with pressure springs to have the same cutting conditions. Cutting conditions in terms of speed, pressure, and depth of cut cannot be provided.

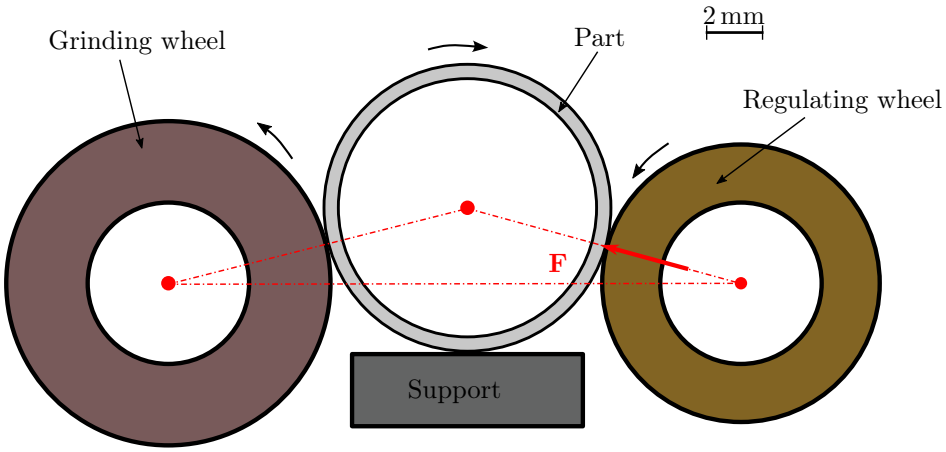


Figure 2: Sketch of outer grinding by centerless in end-feed configuration. Only the pressing force **F** is represented.

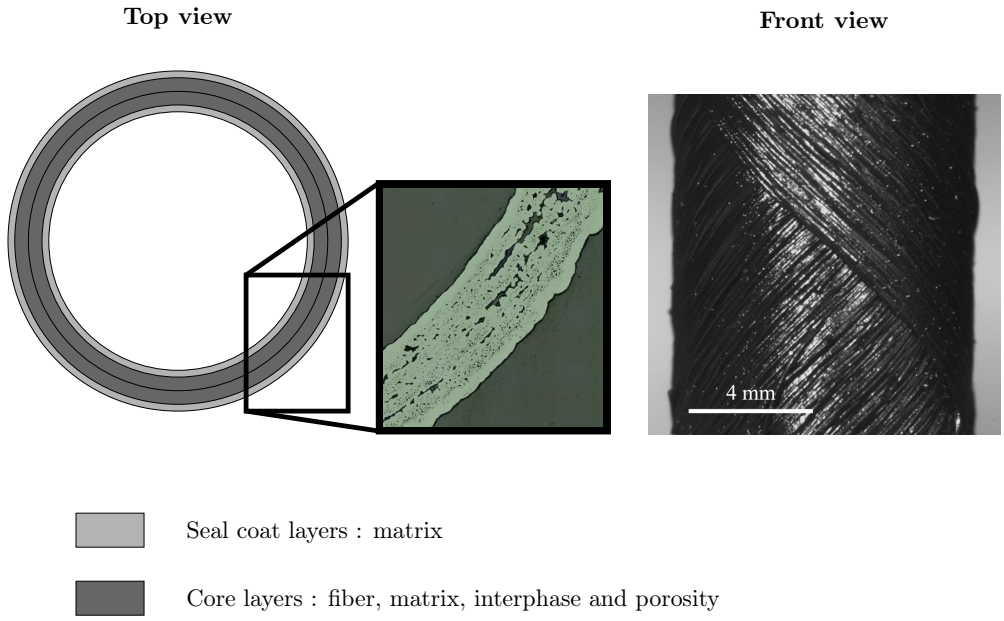


Figure 4: Sketch of the architecture of SiC/SiC tubes.

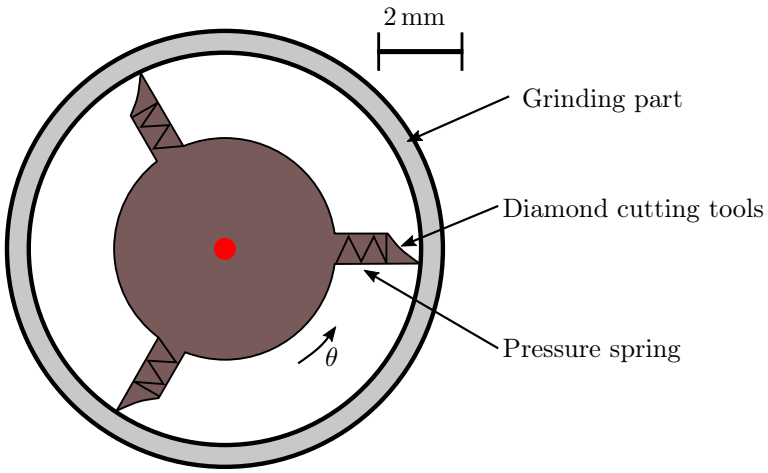


Figure 3: Sketch of inner grinding.

## 2.2 Description of the microstructure of CVI-SiC/SiC composite

The reference tubes can be described in four layers: two core layers and two seal coat layers (Figure 4). The core comprises two layers, corresponding to the two filament wound layers at ±45°. They are formed of matrix, fibers, and porosity. They have an orthotropic behavior. The inner and outer seal coat layers are made of matrix only. They have an isotropic behavior.

Five grades were manufactured to examine the influence of grinding, surface quality, and seal coat thickness on the macroscopic behavior. The first grade, RR (for raw CVI on outer and inner surfaces), was raw CVI tubes (Figure 5a and Figure 6a). It was considered as the reference grade for this paper, although this grade is not representative of the geometry of industrial fuel cladding. Then, three grades were manufactured with variable inner and outer grinding levels, referred to as OI, O+I, and O+I+ (Figure 5b, c, and d and Figure 6b, c, and d). The first letter refers to the outer surface, and the second letter to the inner surface. The sign + denotes enhanced grinding that removed the whole of the seal coat layers. Finally, O*I grade with a first grinding step on the outer and inner surface as final OI grade, and subsequent densification on the outer surface and a grinding on the outer surface (Figure 5e and Figure 6e). The double step of densification and grinding enabled to obtain the surface roughness recommended in Deck et al. [8]. Therefore, the grade O*I possesses the closest specifications of nuclear cladding.

The microstructure of the different grades was characterized. In particular, the section area, the seal coat thicknesses, and the volume fraction of fiber, matrix, and porosity in the core were determined with image analysis from both longitudinal and transversal cuts of specimens. The end of the tensile specimen was cut, cold-coated, and polished to observe the material by optical microscopy (VHX Keyence digital microscope with a VH-Z20R/W lens) with a magnification between ×400 and ×600.

The section of each tensile sample was measured at both ends of the tube thanks to binarized cross-section images [35]. At least five specimen were examined and averaged for each grade (Table 1), with the exception of the O*I grade where only three samples were analysed. However, the section used for the mechanical analysis was the average of the upper and the lower section of each considered sample.

In addition, the surface fraction of porosity, fiber, and matrix in the core were measured on two transversal sections, and one longitudinal section of each sample [35]. The volume fraction for each grade was determined and reported in Table 1. The

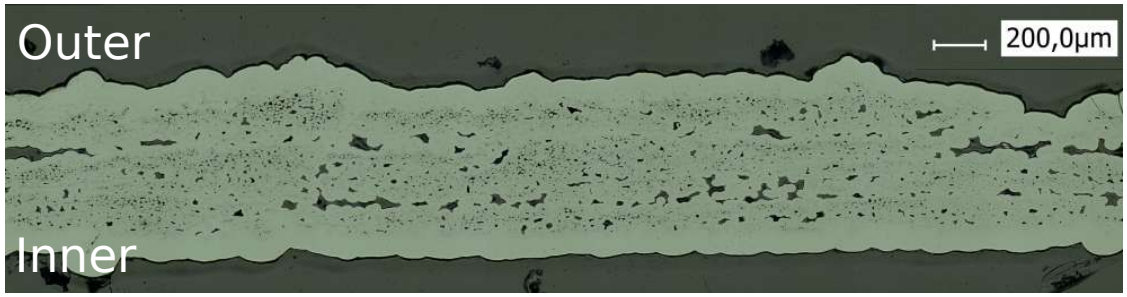


(a) Grade RR

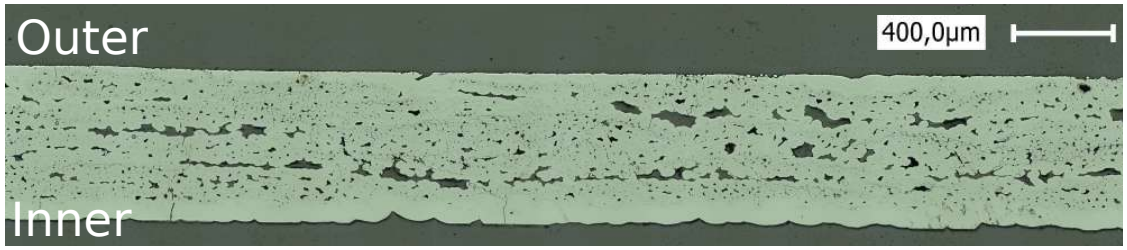


(b) Grade OI


(c) Grade O+I

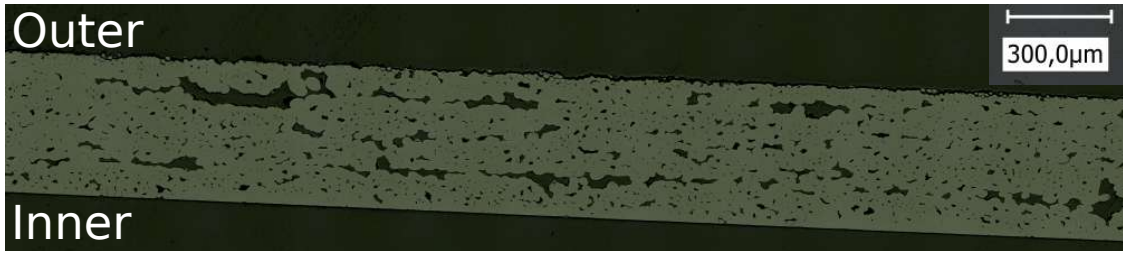


(d) Grade O+I+

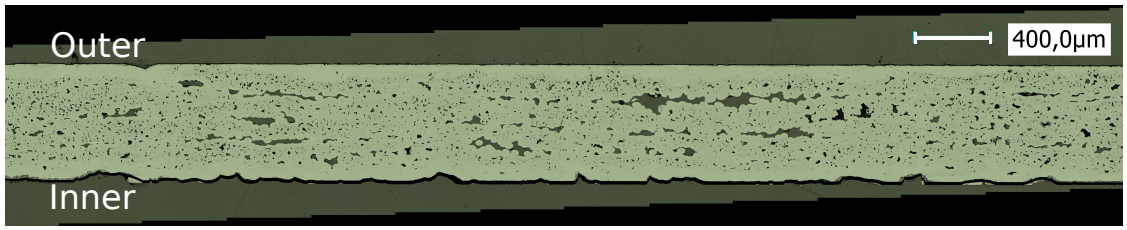


(e) Grade O*I

Figure 5: Longitudinal cuts (along the tube axis of revolution) for the different grades.

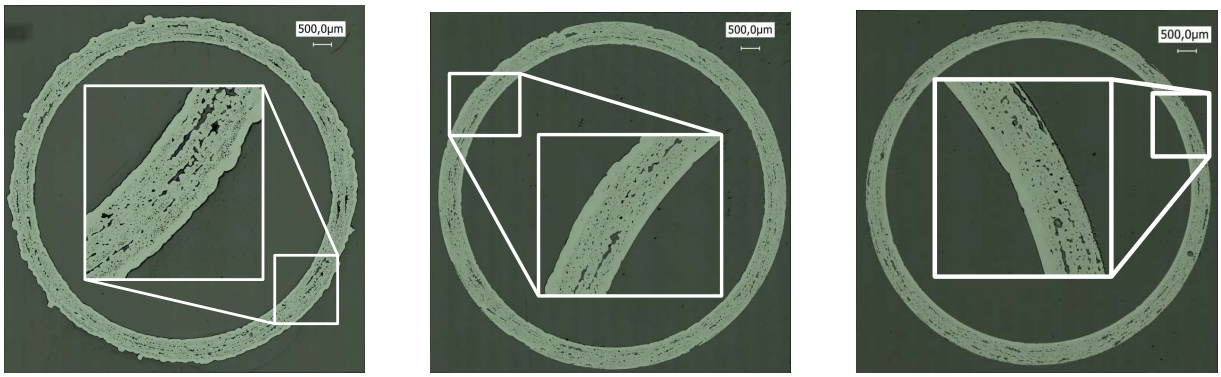


(a) Grade RR (b) Grade OI (c) Grade O+I

(d) Grade O+I+ (e) Grade O*I

Figure 6: Transversal cuts (from the tube axe of revolution) for the different grades.

| Grade | | RR | OI | O+I | O+I+ | O*I |
|---|---|---|---|---|---|---|
| Section $S_O$ | | 18.96 mm$^2$ | 16.63 mm$^2$ | 13.42 mm$^2$ | 12.06 mm$^2$ | 16.1 mm$^2$ |
| Core | Fiber fraction | 36.7 % | | | | |
| | Porosity fraction | 9.1 % | | | | |
| | Matrix fraction | 54.2 % | | | | |
| Seal coat | Inner thickness | 58 µm | 61 µm | 57 µm | 0 µm | 34 µm |
| | Outer thickness | 84 µm | ≈ 30 µm | 0 µm | 0 µm | 48 µm |
| Roughness | Inner $R_a$ | 11.3 µm | 10.6 µm | 10.9 µm | 2.0 µm | 10.9 µm |
| | Inner $R_t$ | 125 µm | 92 µm | 105 µm | 51 µm | 98 µm |
| | Outer $R_a$ | 32.5 µm | 2.4 µm | 3.0 µm | 4.6 µm | 0.9 µm |
| | Outer $R_t$ | 257 µm | 48 µm | 38 µm | 61 µm | 18 µm |

Table 1: Characterization of the different grades : section, core composition, seal coat thickness and roughness (average roughness $R_a$ and maximum roughness $R_t$ [38]).

composition of the core of each grade was identical, i.e., $v_f$=36.7 % of fiber, $v_m$=54.2 % of matrix and $v_p$=9.1 % of porosity of the core volumetric content.

The seal coat thicknesses on inner and outer surfaces were locally measured on both the longitudinal and transversal observations at least on six points on each images [35]. Because of the reference tubes outer surface irregularities and the irregularity of core layers (Figure 7), the seal coat thickness can present a high variation after the grinding process. Only average thicknesses are given in Table 1.

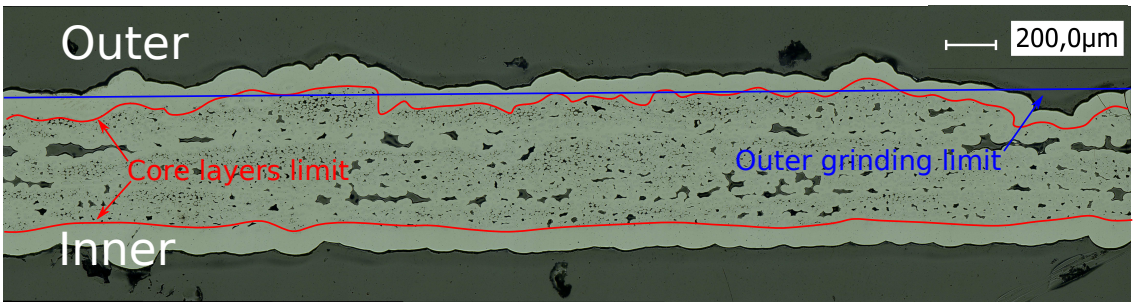


Figure 7: Illustration of waviness defects (at macroscopic scale) on the outer surface on grade RR.

The surface roughness was measured with the roughness tester Mahr (Driveunit GD 120). The roughness was measured on a generator parallel to the tube axis over a length of 55 mm. Six measurements on three generators at 120° on two samples enabled the determination of the average roughness of the five grades. Table 1 gives the average roughness $R_a$, and maximum roughness $R_t$ of each grade [38].

The reference grade, RR, possessed a 58 µm thickness inner seal coat. The first inner grinding step (noted I) did not modify the inner seal coat thickness, i.e., the thickness of OI and O+I grades were respectively 61 µm and 57 µm. This step did not have a significant influence on average roughness (11.3 µm for RR against 10.6 µm for OI and 10.9 µm for O+I on the inner surface). However, this step enabled the reduction of the total roughness (125 µm for RR against 92 µm for OI and 105 µm for O+I on the inner surface). Indeed, only the major defects were removed at this step, as it can observed on Figures 5 and 6. The entire inner seal coat layer was removed on grade O+I+. This operation enabled reduction of the average and total roughness values.

The fibrous preform was prepared around a cylindrical mandrel. The inner surface was directly wound on the mandrel, so it had a smooth surface. The outer surface possesses the different defects due, in particular, to the stacking of the filament winding layers. The outer surface presents a wavy shape (Figure 7). On RR tubes, the average and total roughnesses were higher on the outer surface than on the inner surface. The roughness of the outer surface was decreased thanks to both grinding operations: O and O+. Indeed, the average roughness was 32 µm for grade RR against approximately 3 µm for grade OI, O+I, and O+I+. The total roughness was 257 µm for grade RR against approximately 50 µm for grade OI, O+I, and O+I+. Only a part of the outer seal coat layer was removed on grade OI. The core layers with the presence of uncovered fibers were present in some areas, while in others, a seal coat layer was found, as shown in Figure 5b. On grades O+I and O+I+, the entire outer seal coat was removed. However, these differences did not influence roughness. Finally, on grade O*I, the average and total roughness values were reduced compared with other grades thanks to the double densification-grinding steps. The defects linked to the fibrous preform manufacturing were erased. We can also notice a thin seal coat layer on the inner surface of the O*I grade compared to OI and O+I.

Finally, the first observations indicated that there were no particular new cracks due to the grinding process (Figure 8).

## 2.3 Mechanical tests protocol

Cyclic tensile tests were performed up to failure on 70 mm long samples. The plies orientation at ±45° generated a local loading of the material in tensile-shear. The tests were performed according to ISO 20323 standard [39]. Tube ends were bonded to collars using an epoxy adhesive glue (3M Scotch-Weld$^{TM}$ 9323 B/A) in order to guarantee that the tubes were aligned with the direction of tension. The specimens were then mounted onto the gripping system on the tensile machine (Shimadzu Autograph AGS-100kNX). The lower-end collar was fixed with adhesive to the passive grip, whereas the upper-end collar was screwed on the upper grip. The experimental setup is shown in Figure 9.

During the tensile test, the cross head displacement was controlled at a constant rate of 0.005 mm/min. The force measurements were performed by a 100 kN force cell ( Shimadzu 1220 AJ). The deformations were measured using a longitudinal class 1 extensometer (Epsilon 3442-U10M-U10M-ST) of 25 mm gauge length. An acoustic emission sensor (VS700-D by Vallen System) and a signal conditioner and data acquisition system (AMSY6) were used. The acoustic emission sensor was fixed onto the upper-end collar.

Cyclic tensile tests were performed, with less than five cycles carried out, including the first cycle in the elastic domain. Cycle loading were initiated at defined stress thresholds. Unloading started at the stress thresholds of 50 MPa, 150 MPa, 200 MPa, 250 MPa and 300 MPa, down to a compressive stress of −50 MPa, to cause matrix cracks closure. Figure 10 shows the evolution of the load as a function of time for a representative test of the reference grade RR.

# 3 Analysis of the mechanical behavior

## 3.1 Elastic behavior

The elastic modulus $E$ was calculated by linear regression on the first unloading-reloading cycle (from 0 MPa to 50 MPa with a return to compression at −50 MPa) (Figure 11). The absence of acoustic emission events confirmed that no crack was created within that stress range (Figure 12).

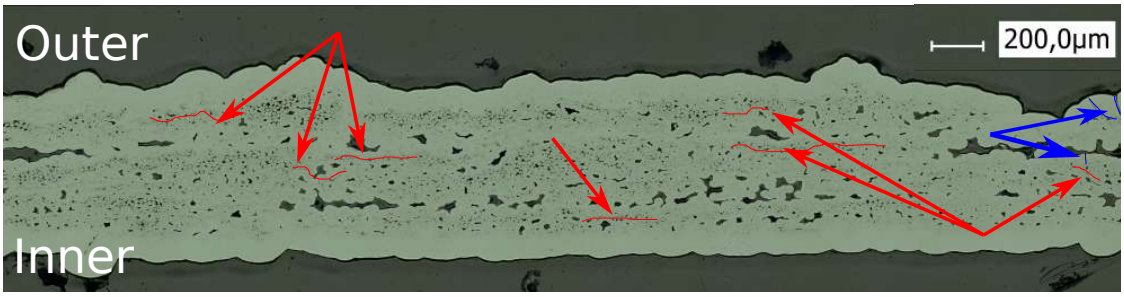


(a) Grade RR

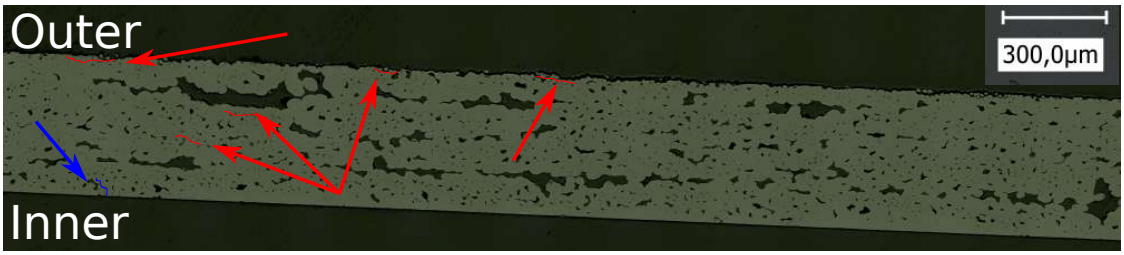


(b) Grade O+I+

Figure 8: Initial observation at digital microscope Keyence on raw CVI tube (i.e., RR grade on Figure a) and grinding tube (i.e., grade O+I+ on Figure b). The cracks perpendicular to the tube axis are highlighted in red, and the cracks parallel are highlighted in blue.

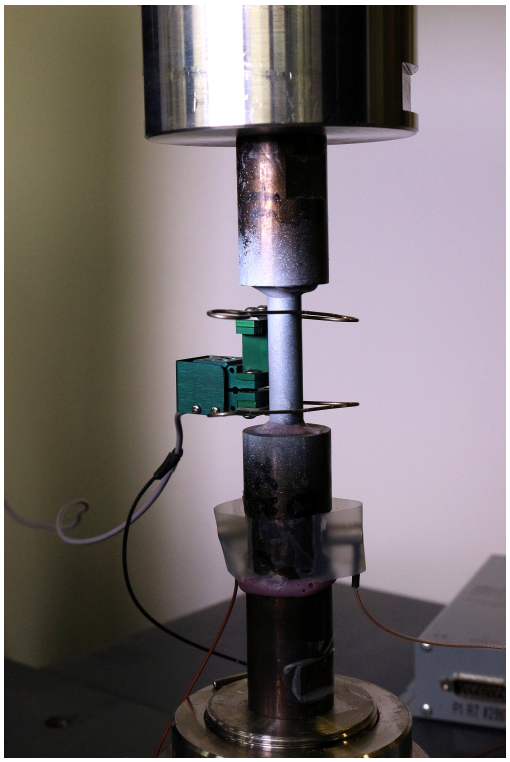

Figure 9: Tensile test experimental device.

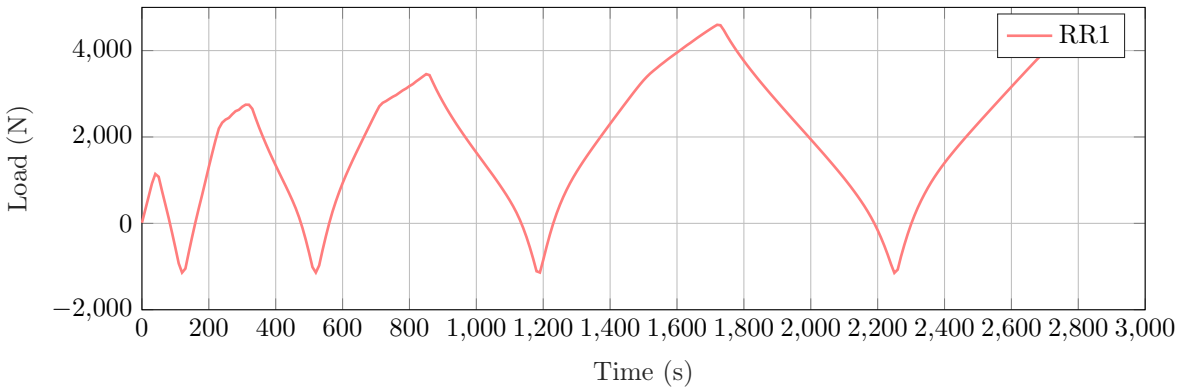


Figure 10: Evolution of the load as a function of time for a representative test of the reference grade RR.

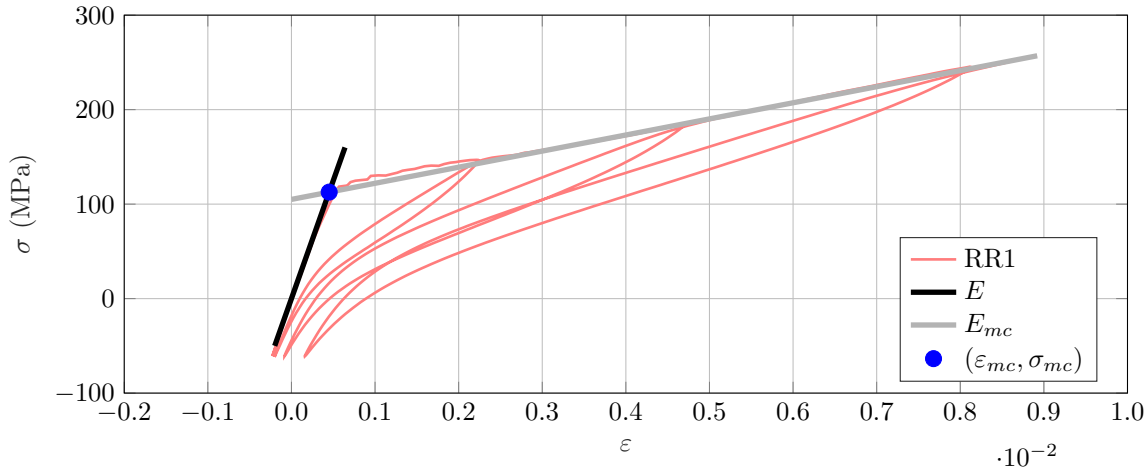


Figure 11: Method for the construction of elastic modulus $E$, tangent modulus $E_{mc}$ and intersection $(\varepsilon_{mc}, \sigma_{mc})$ for a sample of RR grade.

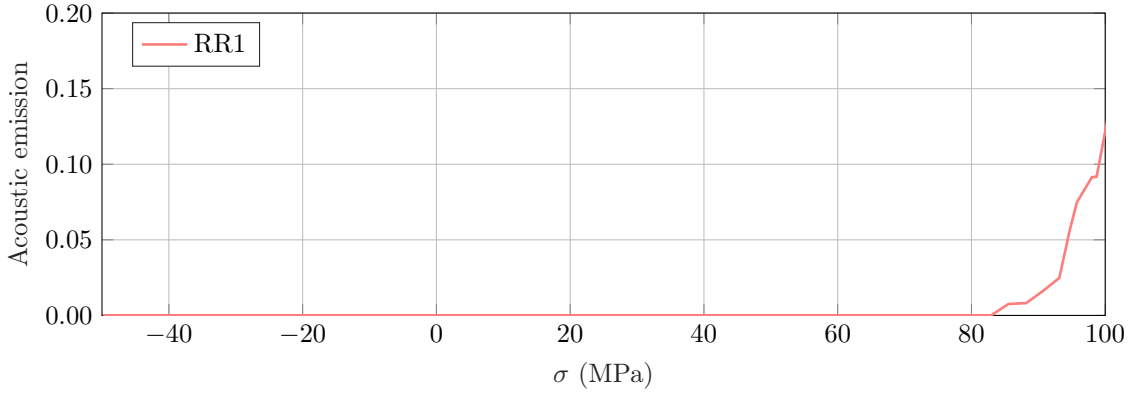


Figure 12: Normalized acoustic emission as a function of the stress on sample RR during the first unloading-reloading cycle.

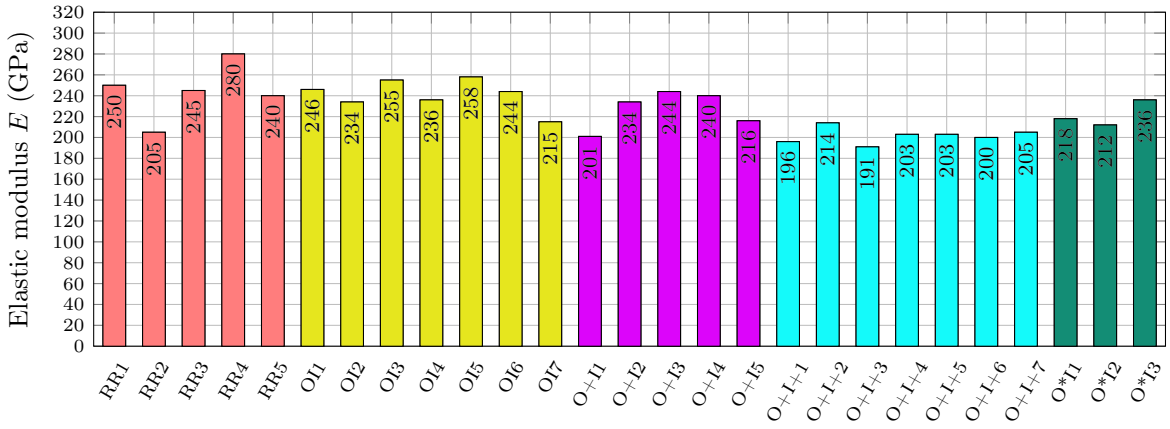


Figure 13: Elastic modulus $E$ for the different samples.

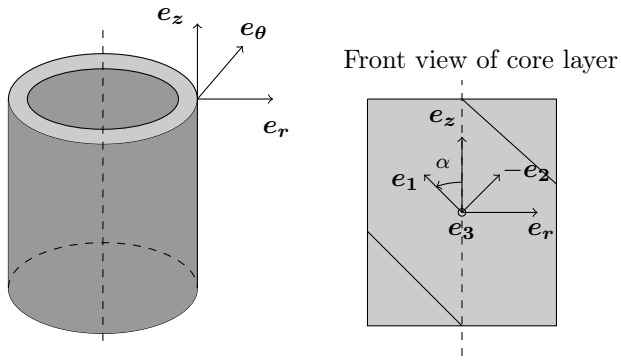


Figure 14: Definition of the different bases of the material.

Figure 13 presents the elastic modulus of the five grades. The experimental standard deviation was between ±3.5 % and ±7.0 %. The variation coefficient was ±5 %. The elastic modulus decreased when the seal coat thickness was removed. The reference raw CVI grade (RR) presents an average elastic modulus $E$ =244 GPa against $E$ =202 GPa for the grade O+I+ without seal coat. However, the experimental results were insufficient to determine if the decrease of elastic modulus was due to the modification of matrix volume fraction in the sample or if to a pre-damage linked to the grinding process.

An elastic analytical model was implemented to determine the grinding process effect on mechanical behavior. The elastic analytical model is based on continuum mechanics. Four layers model the material: two seal coat layers on the outer and inner surface and two core layers (Figure 4). The interfaces between the layers are supposed to be perfect, and the outer and inner surfaces are considered free. A load was applied at the ends of the tube, on tube axis $\mathbf{e_z}$. The seal coat layers are composed of the SiC matrix; the behavior is considered isotropic. The numerical values are taken from Buet et al. [36] and given in Table 2. The core layers are made of matrix, fibers, and porosity. The mechanical behavior is considered to be orthotropic. The mechanical behavior of the core layers is determined in the plies bases, oriented at ±45°. There are two core layers, one oriented at −45° and the other at +45° (Figure 14). The construction of the mechanical tensor of a core layer is done in three steps. First, only the isotropic matrix was considered. Second, the effect of porosity was added. Classical homogenization models (Voigt, Reuss, Hashin-Strikman) have been tested to determine the elastic properties, but they did not represent the elastic behavior of core layers. Probably, the assumptions on porosity shape (ellipsoidal) were too strong to predict the elastic behavior. The porosity was modeled by making an analogy with the mesocraking behavior [40]. This model allows the separation of the porosity effect on elastic behavior in the three space directions and so taking into account the variety of orientations and shapes of porosity at a macroscopic scale. Therefore, this model allows taking into account the orientation and the anisotropy of the porosity. Finally, the fiber behavior was added only in the fiber direction $\mathbf{e_1}$ by modifying the elastic modulus in this direction using a mixture law. The numerical values for fiber properties were extracted from Buet et al. [36] and given in Table 2.

The analytical elastic moduli of the different grades were calculated as a function of the geometrical characteristics given in Table 1. The model gives a satisfactory prediction of the elastic modulus of the different grades (Table 3). Indeed, the model error is always included in the standard deviation or in the measurement error. Therefore, the grinding process and the second

| Parameters | Numerical values |
|---|---|
| $E_m$ | 416 GPa |
| $E_f$ | 374 GPa |
| $\nu_m$ | 0.19 |

Table 2: Parameters for the elastic analytical model (data extracted form [36]).

| Grade | RR 5 samp. | OI 7 samp. | O+I 5 samp. | O+I+ 7 samp. | 0*I 3 samp. |
|---|---|---|---|---|---|
| $E$ (GPa) | $244_{\pm 17}$ | $241_{\pm 15}$ | $227_{\pm 15}$ | $202_{\pm 7}$ | $223_{\pm 12}$ |
| Model $E_{mod}$ (GPa) | 252 | 236 | 228 | 199 | 233 |

Table 3: Comparison of experimental average elastic modulus and analytical young modulus. The standard deviation is given as an index for each grade.

| Grade | RR 5 samp. | OI 7 samp. | O+I 5 samp. | O+I+ 7 samp. | O*I 3 samp. |
|---|---|---|---|---|---|
| $E_{mc}$ (GPa) | $17.3_{\pm 0.6}$ | $18.7_{\pm 0.3}$ | $18.0_{\pm 0.5}$ | $15.1_{\pm 0.7}$ | $18.7_{\pm 0.9}$ |

Table 4: Tangent modulus $E_{mc}$ for the different grades. The standard deviation is given as an index for each grade.

densification-grinding step did not induce predamage to the material, as suggested by microstructure observations. The decrease of elastic moduli with the grinding steps is only due to a modification of the global volume of the matrix respective to fiber and porosity.

## 3.2 Damage behavior with unloading-reloading cycles

### 3.2.1 Transition between elastic and damage behaviors and global indicator of damage evolution

To start with damage behavior analysis, a global indicator of the damage behavior was proposed. This indicator is the tangent modulus of the damage part of the tensile envelope curve, named $E_{mc}$ in the following (Figure 11). This modulus was determined by linear regression between 150 MPa and ultimate failure on the envelope of the curve (red in Figure 11). The linear regression coefficient $R^2$ for all samples was superior to 0.99. This tangent modulus characterizes the damage phenomenon that occurs as a result of matrix cracks, the saturation of matrix, fiber cracks, slippage at fiber/matrix interphase, and also at plies scale. This $E_{mc}$ modulus is also an indicator of the global damage kinetics.

Table 4 presents the average experimental tangent modulus $E_{mc}$ for the different grades, and Figure 24 in A presents all the values for the samples. The first grinding process, with the OI and O+I grade, induced an increase of tangent modulus $E_{mc}$ in comparaison with the RR grade ($E_{mc}$ =18.7 GPa for OI, $E_{mc}$ =18.0 GPa for O+I against $E_{mc}$ =17.3 GPa for RR). The damage evolution was slower than that of the reference RR grade, particularly on the OI grade. The important grinding step of the inner seal coat, with the O+I+ grade, implied a decrease of tangent modulus $E_{mc}$ and increased damage speed. Indeed, grade O+I+ presented a tangent modulus $E_{mc}$ =15.1 GPa against $E_{mc}$ =17.3 GPa for reference grade RR and $E_{mc}$ =18.0 GPa for grade O+I, which differed by the inner seal coat layer. The grade O*I presented a tangent modulus similar to grades OI and O+I. Therefore, the roughness did not seem to affect damage kinetics.

The intersection between the elastic curve having $E$ slope and the damage curve with $E_{mc}$ slope indicates the deformation or the stress at the transition between elastic domain and the matrix cracking, labeled respectively $\varepsilon_{mc}$ and $\sigma_{mc}$. An example of the determination of both indicators is given in Figure 11. Table 5 presents the average experimental strain $\varepsilon_{mc}$ and stress $\sigma_{mc}$ for the different grades, and Figure 25 and 26 in A present the values of all the samples. The grinding steps did not influence the stress $\sigma_{mc}$, because of the difference in rigidity of the different grades. The strain $\varepsilon_{mc}$ increases when seal coat thickness decreases. The main assumption is that the SiC grains deposited by CVI have a specific microstructure, particularly on the seal coat layers. The SiC specific microstructure may consist of a sizeable columnar arrangement, making them brittle, particularly along the intercolumnar directions of SiC grains [41]. Thus, the seal coat layers probably crack first, explaining why that grades with less seal coat thickness presented a larger strain $\varepsilon_{mc}$. Another explanation is based on the strength dependence on volume, the strength increases when the volume decreases because the probability of existence of a critical flaw decreases.

Variation of the tangent modulus allowed the determination of different kinetics of damage in function of the surface quality and seal coat thickness. However, the link with the damage mechanism was not established.

### 3.2.2 Unloading and reloading cycle analysis

The unloading-reloading cycles can provide further information on damage phenomena in the composite. A large number of models, all based on shear-lag assumption, were developed in order to study the unloading-reloading cycles in the case of unidirectional composites [30, 31, 42]. The loading direction was parallel to the fibers for unidirectional composites. For filament wounded tube at ±45°, locally, the plies are loaded in traction (along the fiber direction) and shear. Aveston et al. [43] studied the influence of fiber orientation as a function of cracks direction. The load on interface depends on fiber orientation. However, the damage mechanisms are similar whatever the fiber orientation. Therefore, the methodology of analysis of unloading-reloading cycles on the tube was inspired by the methodology developed by Domergue, and Vagaggini [30, 31] on unidirectional composites (Figure 15). Four indicators were used directly from Domergue and Vagaggini [30, 31]:

- the tangent compliance at the beginning of unloading $1/E^*$;

| Grade | RR 5 samp. | OI 7 samp. | O+I 5 samp. | O+I+ 7 samp. | 0*I 3 samp. |
|---|---|---|---|---|---|
| $\varepsilon_{mc}$ (%) | $0.046_{\pm 0.002}$ | $0.050_{\pm 0.003}$ | $0.055_{\pm 0.004}$ | $0.063_{\pm 0.003}$ | $0.058_{\pm 0.004}$ |
| $\sigma_{mc}$ (MPa) | $113_{\pm 3}$ | $120_{\pm 2}$ | $124_{\pm 1}$ | $127_{\pm 3}$ | $123_{\pm 3}$ |

Table 5: Strain $\varepsilon_{mc}$ and stress $\sigma_{mc}$ for the five grades. The standard deviation is given as an index for each grade.

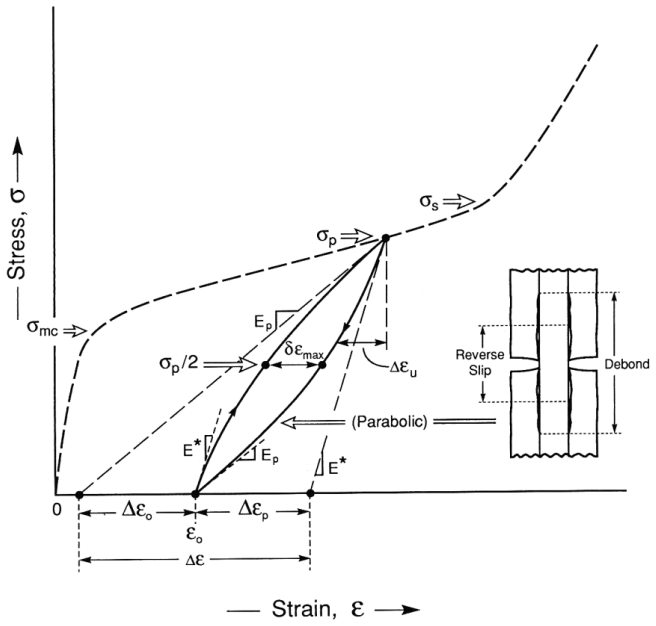


Figure 15: Sketch of cyclic tensile test on unidirectional composite (Illustration extracted from [30]).

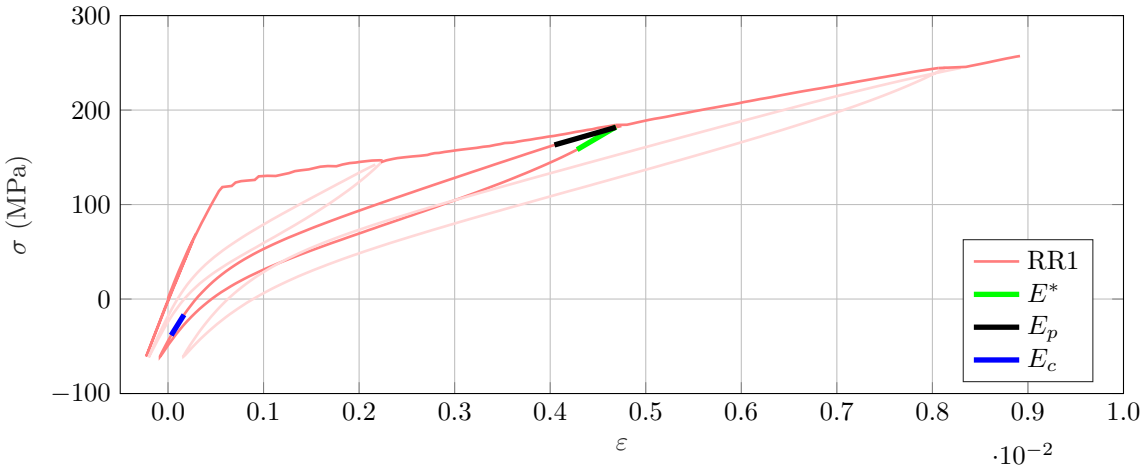


Figure 16: Construction of tangent modulus $1/E^*$, $1/E_p$ and $1/E_c$ for a cycle of grade RR.

- the tangent compliance at the end of reloading $1/E_p$;
- the cycle width at half-height $\delta\varepsilon_{max}$ (i.e., for $\sigma = \sigma_p/2$ with $\sigma_p$ the maximum stress of cycle)
- the area $\mathcal{A}$ of the cycle.

The tangent compliances $1/E^*$ and $1/E_p$ describe damage in the loading direction, i.e.,they reflect the modification of the tangent modulus due to cracks of $\mathbf{e_z}$ normal (tube axis of revolution). The tangent compliance $1/E^*$ and $1/E_p$ were determined by linear regression on each cycle, on a 20 MPa stress range. The slippage is characterized by the cycles width at half-height $\delta\varepsilon_{max}$ or by the area $\mathcal{A}$ of the cycles. Indeed, no cracks were created during a cycle, as shown by the acoustic emission curve in A Figure 27. Therefore, the hysteresis was attributed to slippage. In the case of an unidirectional composite, the slippage occurs at the fiber/matrix interface. Slippage during tensile tests on tubes can also occur at the plies length scale with the slight reorientation of the plies [10].

Additionally to Domergue and Vagagini parameters, the compliance at the beginning of reloading $1/E_c$ was measured by linear regression between −40 MPa and −20 MPa. Thanks to the return in compression during a cycle, the cracks perpendicular to the loading direction were closed. Therefore, the compliance $1/E_c$ characterizes the shear damage, i.e., the modification of the tangent modulus due to cracks of $\mathbf{e_r}$ normal.

**Damage in the loading direction** Figure 17 and Figure 18 present the evolution of the tangent compliance $1/E_p$ and $1/E^*$ for the different samples as a function of the strain $\varepsilon_p$ (maximum strain of the cycle). No significant differences were observed between the different grades. The acoustic emission curves confirmed the same kinetics of crack evolution between the different grades (Figure 27 in A). Therefore, damage in the tensile direction was mainly driven by the core layers.

A sensitivity analysis of the stiffness loss in function of the core and seal coat layers behavior was proposed to explain why the core drives damage in the tensile direction. Only a two-layers composite was considered to simplify the analysis. The first

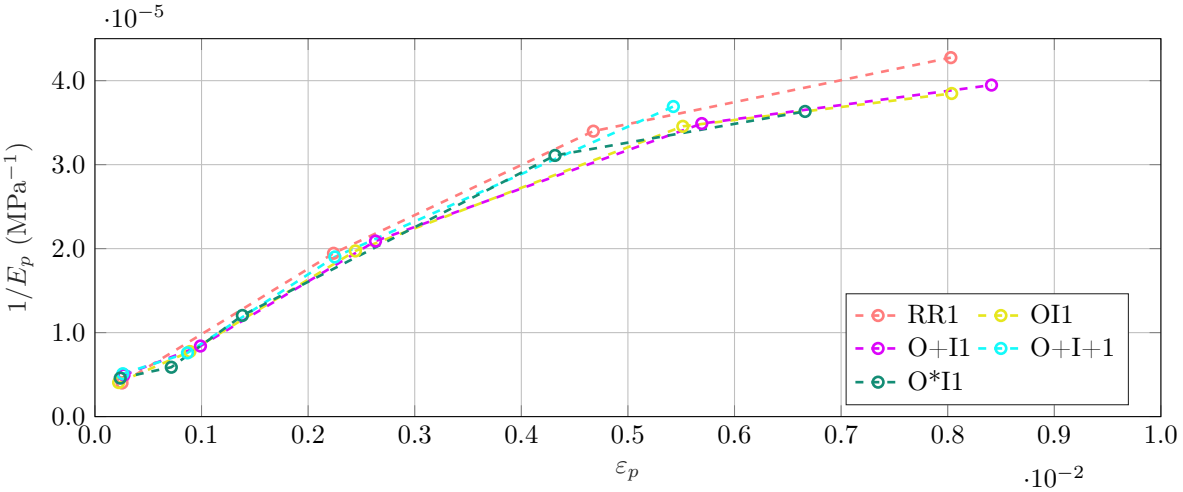


Figure 17: Evolution of the tangent compliance $1/E_p$ as a function of the strain for representative sample of each grades.

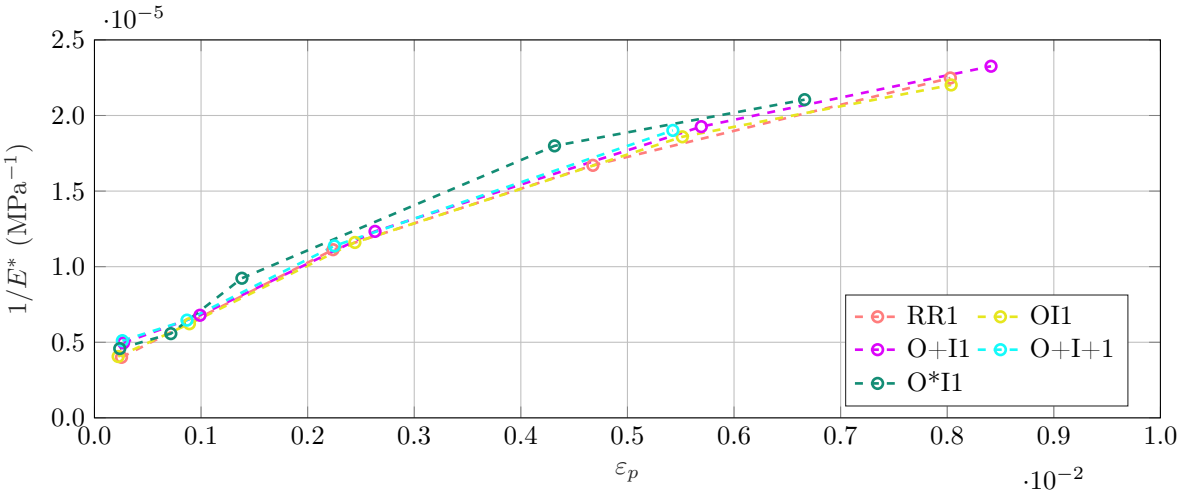


Figure 18: Evolution of the tangent compliance $1/E^*$ as a function of the strain for representative sample of each grades.

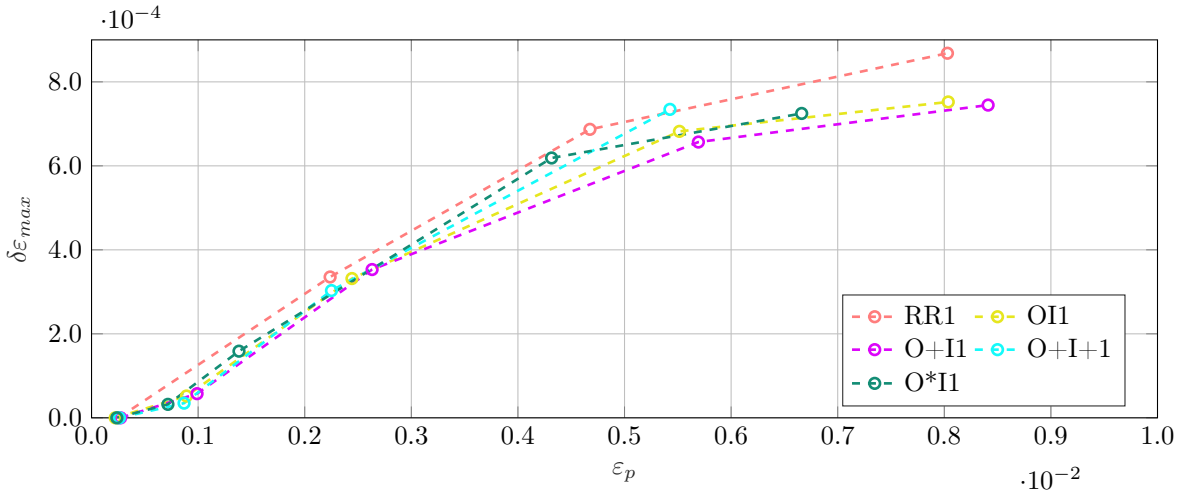


Figure 19: Evolution of the cyclic width at half-height $\delta\varepsilon_{max}$ as a function of the strain for representative sample of each grades.

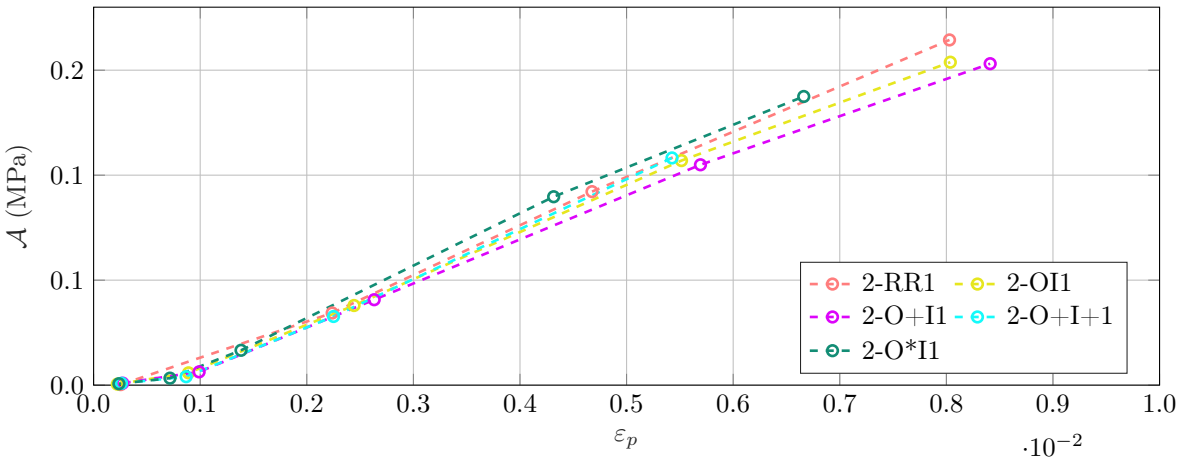


Figure 20: Evolution of area $\mathcal{A}$ of the cycle as a function of the strain for representative sample of each grades.

layer, noted by $\bullet_{sc}$, corresponds to the seal coat layers, and the second layer, noted by $\bullet_c$, corresponds to core layers. The force $N$ applied to the sample is related to the strain $\varepsilon$ by the cross-section $S_{sc}$ or $S_c$, damage $d_{sc}$ or $d_c$ defined by Lemaitre et al. [44], and the initial elastic modulus $E^0_{sc}$ or $E^0_c$ of each layer :

$$N = \Big(S_{sc}E^0_{sc}(1-d_{sc}) + S_cE^0_c(1-d_c)\Big)\varepsilon. \tag{1}$$

The average damage is

$$\bar{d} \quad = \quad 1 - \frac{S_{sc}E^0_{sc}(1-d_{sc}) + S_cE^0_c(1-d_c)}{S_{sc}E^0_{sc} + S_cE^0_c}. \tag{2}$$

By applying a Taylor series of $\alpha$, then damage $\bar{d}$ is

$$\bar{d} \quad \approx \quad d_c + \alpha(d_{sc} - d_c) \quad \text{with} \quad \alpha = S_{sc}E^0_{sc}/S_cE^0_c. \tag{3}$$

Thus, the average damage of the tubes corresponds to the damage of the core in the first order, followed by the seal coat layers. Furthermore, as seen previously, the seal coat layers seem to crack before the core layers. Therefore, the seal coat certainly has a minimal role in the mechanical behavior of the tubes on the damage in tensile behavior. This was expected by owing to the fact that the core plays the role of reinforcement of the tube.

**Slippage** Figure 19 and Figure 20 present the evolution of the cyclic width at half-height $\delta\varepsilon_{max}$ and the area $\mathcal{A}$ of the cycle for the different samples as a function of strain $\varepsilon_p$. As for the tangent compliance $1/E_p$ and $1/E^*$, no significant differences were observed between the grades. The slippage probably occurred at the fiber/matrix interface or between the two orthotropic layers, i.e., the core layers.

**Damage in the shear direction** Figure 21 presents the evolution of the tangent compliance at the beginning of reloading $1/E_c$ as a function of the strain in order to characterize the shear damage. The different grades had different behavior. The slope $\dot{D}_c$ of the evolution of the tangent modulus $1/E_c$ as a function of strain was determined to characterize the shear

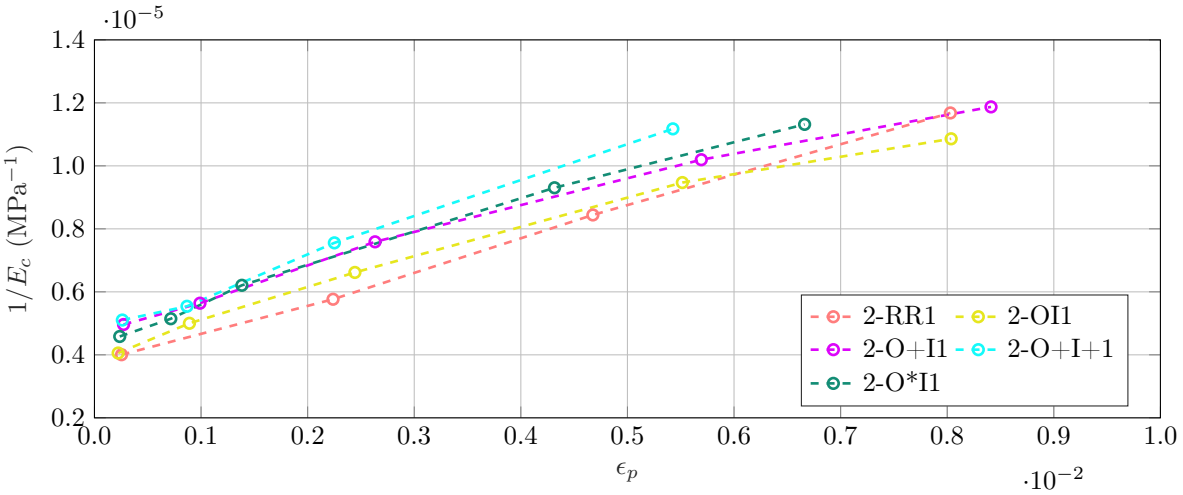


Figure 21: Evolution of the tangent compliance $1/E_c$ as a function of the strain for representative sample of each grades.

| Grade | RR $_{5\ \text{samp.}}$ | OI $_{7\ \text{samp.}}$ | O+I $_{5\ \text{samp.}}$ | O+I+ $_{7\ \text{samp.}}$ | O*I $_{3\ \text{samp.}}$ |
|---|---|---|---|---|---|
| $\dot{D}_c$ (MPa$^{-1}$) | $4.6.10^{-4}{}_{\pm 4.10^{-5}}$ | $3.8.10^{-4}{}_{\pm 3.10^{-5}}$ | $4.2.10^{-4}{}_{\pm 2.10^{-5}}$ | $5.6.10^{-4}{}_{\pm 10.10^{-5}}$ | $4.4.10^{-4}{}_{\pm 3.10^{-5}}$ |

Table 6: Average shear damage speed $\dot{D}_c$ for the different grades. The standard deviation is given as an index for each grade.

damage rate and to estimate the influence of surface quality and seal coat thickness on the evolution of shear damage. Table 6 presents the average shear damage speed $\dot{D}_c$ for all grades, the Figure 28 in A shows the shear damage rate $\dot{D}_c$ for all the samples.

The outer grinding steps OI and O+I brought a slight decrease in shear damage rate compared with the reference grade RR. Grinding the significant surface defect probably allowed this decrease. The grade O+I presented a shear damage rate slightly larger than that of grade OI, probably because of the machining of few fibers on the outer surface. The grade O*I presented a shear damage rate equivalent to that of grade OI. Thus, the surface roughness quality seemed to have a minimal influence. Only the grinding of major defects influenced the shear damage.

The shear damage rate of grade O+I+ was greater than that of reference grade RR and grade O+I, which presented the same core and outer seal coat characteristics. Therefore, the inner seal coat presence seems to decrease the shear damage rate. On post-mortem observations, the interface between the core and the outer seal coat layer always showed delamination cracks (in red on Figure 22). It was not the case for the interface between the inner seal coat layer and the core. Thus, the inner seal coat layer can bear a part of the load, whereas the outer seal coat layer can not. Grinding the inner seal coat had more effect on the mechanical behavior than grinding the outer seal coat.

Some assumptions may be proposed to explain the difference in delamination cracking between the inner seal coat and core interface and the outer seal coat and core interface. The elastic behavior analysis demonstrated that inner and outer seal coat layers are subjected to the same macroscopic loading. However, the outer seal coat had waviness defects due to the manufacturing process of the fibrous preform (Figure 7). These defects could locally increase the off-plane load and induce delamination cracks. Another assumption was that the SiC grains structure may differ between the inner and outer seal coat layers [35]. Their mechanical properties could also vary, explaining the crack pattern difference.

**Note** The differences in shear damage rate between the different grades agree with the damage kinetics of the tangent modulus $E_{mc}$. Indeed, when the shear damage rate increased, the tangent modulus $E_{mc}$ decreased, so the damage rate of the envelope increased. Thereby, the envelope evolution was strongly linked to the shear damage evolution.

## 3.3 Failure

Table 7 presents the average strain and stress to failure of each grade. Figure 29 and Figure 30 in A present the results for each sample. The number of tests per grade (between 3 and 7) needs to be increased to make a statistical investigation of the failure. However, the standard deviation of the measurements for the five grades is less than $\pm 4\,\%$ in stress and strain. The results on the fracture values seem to be repeatable and allow us to compare the different grades between them. The failure was delayed when the outer surface was ground. The failure strain increased by $15\,\%$ between the RR and OI grades, where the main outer surface defects had been grounded. The failure occurred at slightly lower stress and strain for O+I compared with OI. The difference may be due to some fiber grinding on the O+I+ grade. However, the difference was not significative for further interpretation. The failure occured at a smaller strain for the O+I+ grade. Indeed, $32\,\%$ strain decrease was observed between O+I+ and O+I grades. The only differences between these grades were the inner seal coat thickness. On O+I, only the main defects were removed, whereas, on O+I+, the entire inner seal coat was removed.

On these four grades: RR, OI, O+I, and O+I+, the failure evolution had the same kinetics as shear damage and tangent modulus $E_{mc}$. When the damage rate increased between two grades, the failure occurred sooner. The inner seal coat seemed to take back a part of the load and delay the ultimate failure.

Moreover, the surface roughness seemed to have a limited impact on failure, as shown by the average stress and strain to failure of the O*I grade. Indeed, despite the better surface quality compared to the OI grade, the failure of the O*I grade

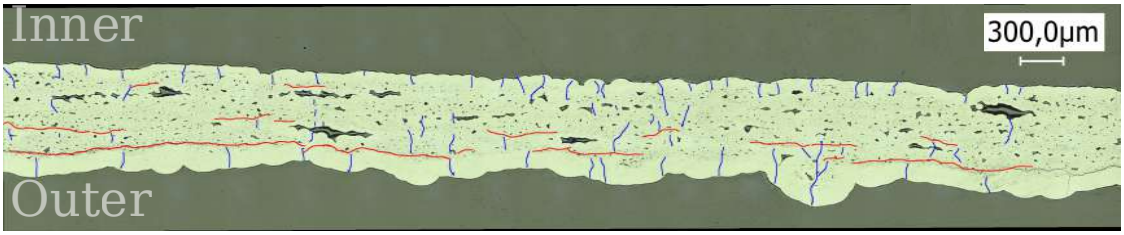


(a) Grade RR

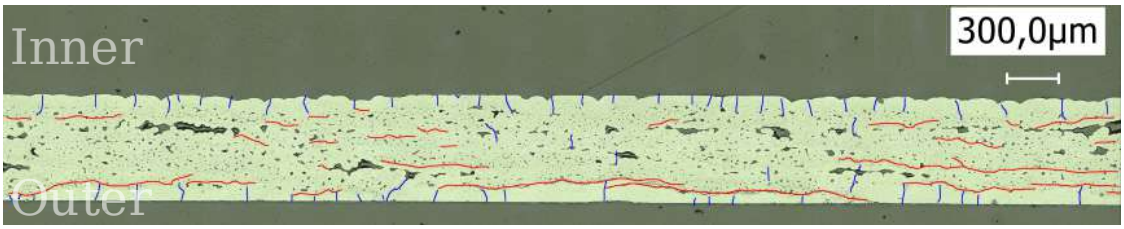


(b) Grade OI

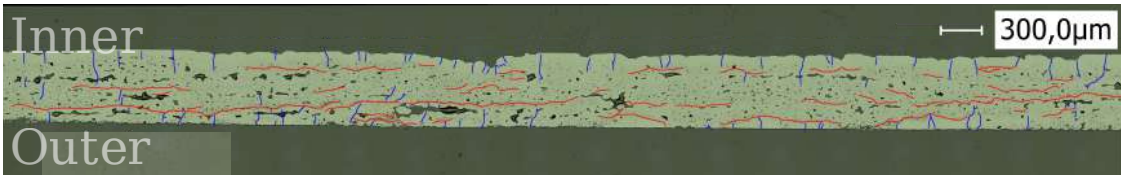


(c) Grade O+I

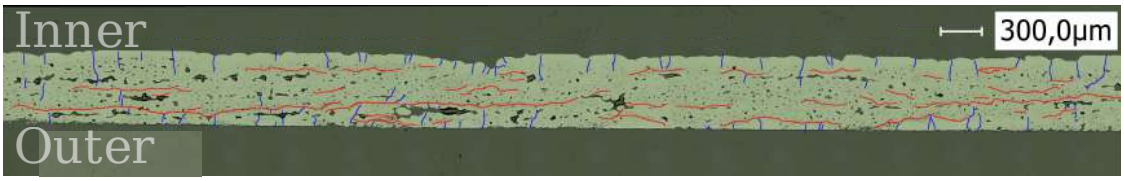


(d) Grade O+I+

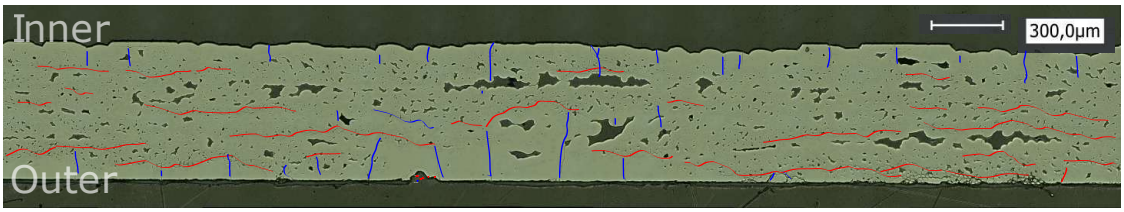


(e) Grade O*I

Figure 22: Post-mortem observations on digital microscope of longitudinal section for a tube of each family. In blue, the cracks perpendicular to the loading direction and in red the cracks parallel to the loading direction.

| Nuance | RR 5 samp. | OI 7 samp. | O+I 5 samp. | O+I+ 7 samp. | O*I 3 samp. |
|---|---|---|---|---|---|
| $\varepsilon_r$ (%) | $0.88_{\pm 0.02}$ | $1.01_{\pm 0.04}$ | $0.98_{\pm 0.04}$ | $0.66_{\pm 0.05}$ | $0.87_{\pm 0, .03}$ |
| $\sigma_r$ (MPa) | $256_{\pm 4}$ | $303_{\pm 9}$ | $292_{\pm 4}$ | $219_{\pm 10}$ | $278_{\pm 11}$ |

Table 7: Average strain and stress to failure for the different grades. The standard deviation is given as an index for each grade.

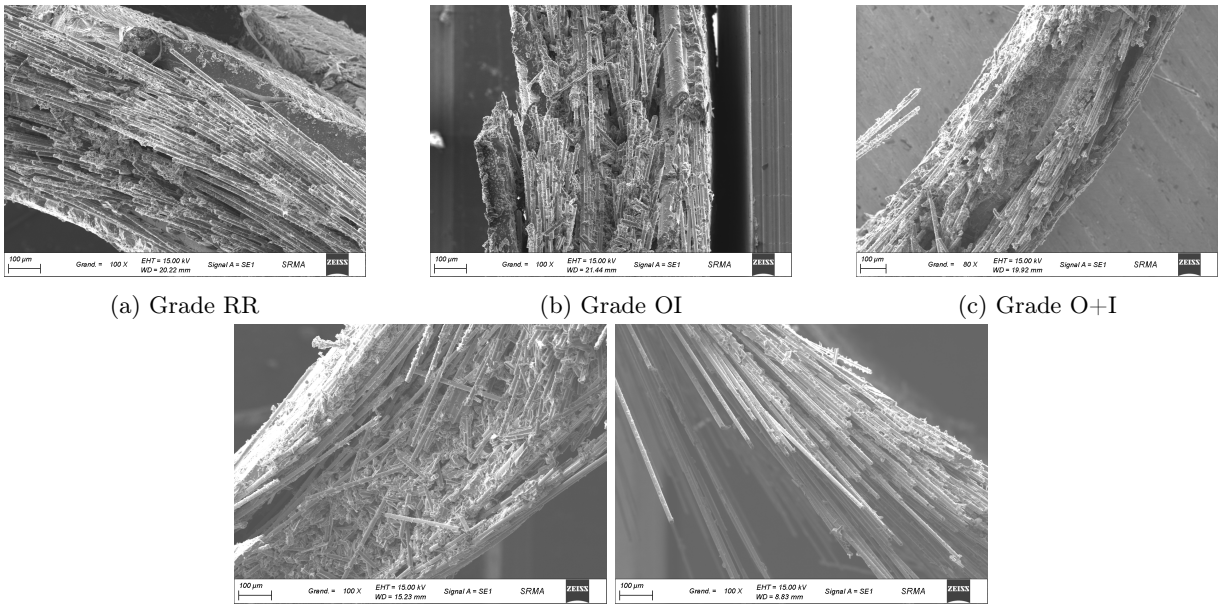

(a) Grade RR (b) Grade OI (c) Grade O+I

(d) Grade O+I+

Figure 23: SEM images of fracture surfaces of all the grades (excepted O*I).

occurred earlier when compared with the OI grade. That was probably due to the thinner inner seal coat thickness of the O*I grade compared to the OI grade.

Figure 23 presents SEM images of the fracture surfaces of RR, OI, O+I, and O+I+ grades. Few differences in fracture patterns were observed between grades RR, OI, and O+I. It was possible to observe areas with fiber/matrix debonding, as shown in Figure 23a, but also areas without fiber/matrix decohesion, as shown in Figure 23c. In these three grades, several directions of debonding were systematically observed in the thickness of tubes. The O+I+ grade had a fracture surface slightly different from the three previous grades (Figure 23d). Zones with long debonding lengths were observed on some parts of the fracture surface. The fracture seemed to be unstable on other parts of the tubes, i.e., without fiber/matrix debonding over almost the entire thickness. Moreover, in the areas of fiber/matrix debonding, the fibers were oriented in a single direction.

The assumption is that the lack of inner seal coat made the load increase on core fibers in comparison to the other grades. If the fibers are more loaded, the decohesion length $L_D$ increases. Indeed, the shear lag model, that describes the evolution of the stress in the matrix and the fibers around matrix cracks [33, 29] gives the following relation :

$$\frac{2\tau L_D}{R_f} = \sigma_m(\infty) - \gamma - \sigma_m^T \tag{4}$$

with $\tau$ the shear stress at interphase, $R_f$ fiber radius, $\gamma$ the stress equivalent to the energy jump at a matrix crack and $\sigma_m^T$ the residual thermal stress, and $\sigma_m(\infty)$ the stress in the matrix far away cracks. The stress $\sigma_m(\infty)$ is proportional to the stress in the fiber $\sigma_f(\infty)$. Large debond lengths were observed on MEB images (Figure 23d). Moreover, because of the heavy load on fibers, the cracks propagated and caused the ultimate failure of the composite. This scenario could explain the smaller stress and strain of failure for the grade O+I+.

# 4 Conclusion

Cyclic tensile tests on SiC/SiC tubes allowed better understanding of the influence of surface quality and seal coat thickness on mechanical behavior. Five grades were studied, with different seal coat thicknesses and surface roughness. Raw CVI tubes were used as the reference grade. Next, several grinding operations were done on the inner and outer surfaces of other tubes.

The analysis of the elastic behavior and the implementation of an analytical model enabled to determine that the surface machining did not predamage the material. The loss of rigidity due to machining was only related to the global decrease of matrix content.

The damage behavior was mainly analyzed thanks to the unloading-reloading cycles using the model proposed on unidirectional composite [30, 31]. Different indicators were introduced: the tangent compliance $1/E^*$ and $1/E_p$ to characterize damage in tensile direction, the tangent compliance $1/E_c$ to characterize damage in shear, and the cycles width at mid-height $\delta\varepsilon_{max}$ and the area $\mathcal{A}$ of the cycle to characterize slippage at fiber/matrix interface scale or plies length scale. The grinding operation and surface quality did not influence damage in the tensile direction nor slippage. The core of the composite seems to drive these

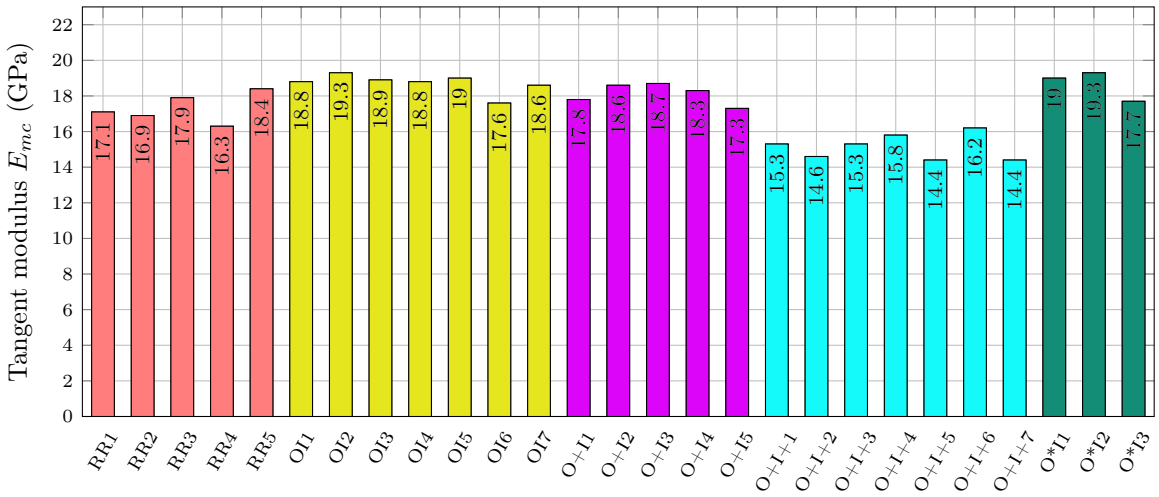


Figure 24: Tangent modulus $E_{mc}$ for the different samples.

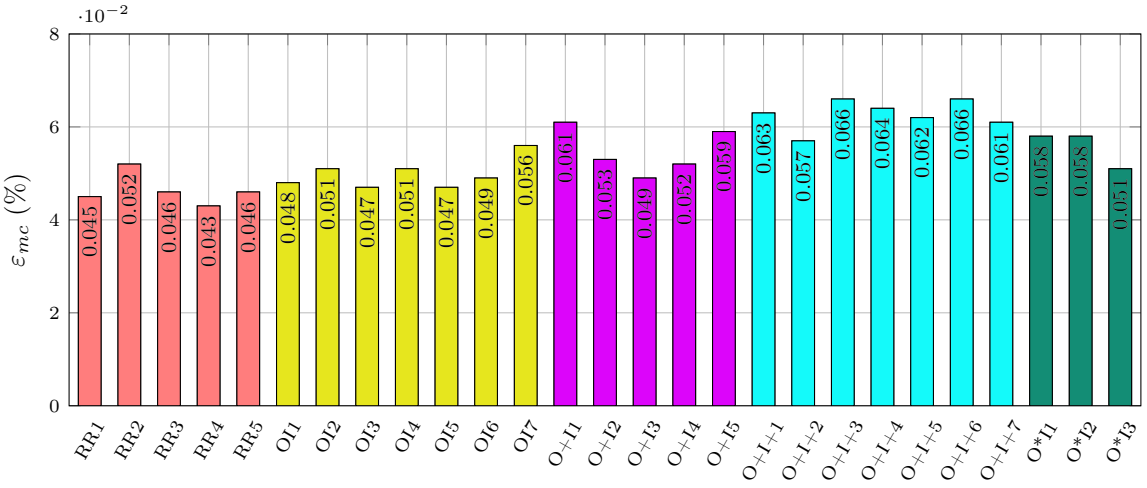


Figure 25: Strain $\varepsilon_{mc}$ for the different samples.

two phenomena. However, the seal coat thickness and, in the second step, the surface roughness influenced the shear damage rate. A slight decrease in damage rate had been observed with the inner machining, i.e., for the OI and O+I grades. Machining of the main surface defects could slow down the damage behavior and delay the failure, mainly if no fiber broke during the grinding process. However, following the roughness tolerance advised by Deck et al. [8] for fuel cladding did not modify the mechanical behavior, as shown by the O*I grade. Inner surface grinding increased the shear damage rate, i.e., for grade O+I+. The micrography analysis after the tensile test demonstrated that the inner seal coat took back a part of the load during the tensile test. In contrast, the outer seal coat presented delamination cracks at the interface with the core layers. Therefore, the outer seal coat had a minor role in the damage behavior.

The evolution of the tangent modulus of the strain-stress curve envelope was similar to that of the shear damage. Indeed, when grade presented a significant shear damage rate, the tangent modulus $E_{mc}$ was softer, meaning with increase of global damage rate. The shear damage also contributed to the ultimate failure of the composite.

This experimental analysis of unloading-reloading cycles, and the unidirectional model enabled us to highlight the significance of the inner seal coat on mechanical behavior. The link between shear damage and the evolution of the envelope of the strain-stress curve had not been fully established. Implementing a numerical model, which considers the tube architecture and the local loading in tensile and shear, will be necessary to understand better the inner seal coat role in the mechanical behavior. This model should consider the geometrical defects related to the manufacturing process to understand the delamination cracks between seal coat and core layers.

# Acknowledgments

This study has been conducted under the French joint Nuclear R&D program between CEA, Framatome and EDF. The authors would like to acknowledge the support provided for the development of new E-ATF cladding solutions in this framework.

# A Complementary experimental data

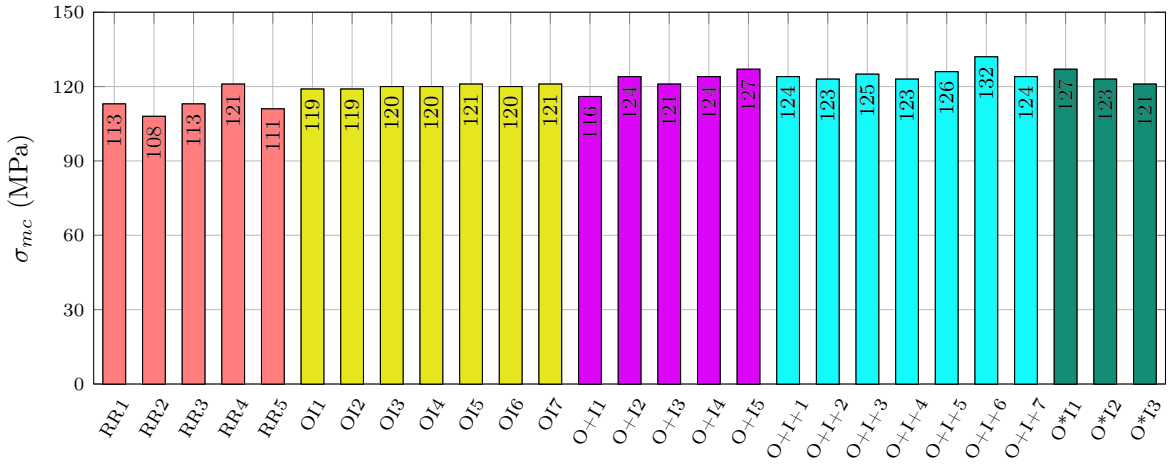


Figure 26: Stress $\sigma_{mc}$ for the different samples.

# References


[1] Y. Katoh, K. Ozawa, C. Shih, T. Nozawa, R. Shinavski, A. Hasegawa, and L. Snead. Continuous SiC fiber, CVI SiC matrix composites for nuclear applications: Properties and irradiation effects. *Journal of Nuclear Materials*, 448(1-3):448–476, 2014.

[2] KA. Terrani. Accident tolerant fuel cladding development: Promise, status, and challenges. *Journal of Nuclear Materials*, 501:13–30, 2018.

[3] L. Snead, Y. Katoh, and T. Nozawa. Radiation effects in sic and sic–sic. *Comprehensive Nuclear Materials*, 2020.

[4] G. H. Seo, G. Jeun, and S. J. Kim. Pool boiling heat transfer characteristics of zircaloy and sic claddings in deionized water at low pressure. *Experimental Thermal and Fluid Science*, 64:42–53, 2015.

[5] C Lorrette, T Guilbert, F Bourlet, C Sauder, L Briottet, H Palancher, J Bischoff, and E Pouillier. quench behavior of sic/sic cladding after a high temperature ramp under steam conditions. In *Water Reactor Fuel Performance Meeting*. Water Reactor Fuel Performance Meeting, 2017.

[6] C Lorrette, C Sauder, P Billaud, C Hossepied, G Loupias, J Braun, A Michaux, E Torres, F Rebillat, JJPotTF Bischoff, et al. Sic/sic composite behavior in lwr conditions and under high temperature steam environment. In *Top Fuel 2015*, 2015.

[7] C. Sauder and C. Lorrette. Patent EP2683673 (CEA): Method for producing a composite including a ceramic matrix, 2012.

[8] CP. Deck, GM. Jacobsen, J. Sheeder, O. Gutierrez, J. Zhang, J. Stone, HE. Khalifa, and CA. Back. Characterization of sic–sic composites for accident tolerant fuel cladding. *Journal of Nuclear Materials*, 466:667–681, 2015.

[9] F. Hashimoto, I. Gallego, J. Oliveira, D. Barrenetxea, M. Takahashi, K. Sakakibara, H. Stålfelt, G. Staadt, and K. Ogawa. Advances in centerless grinding technology. *CIRP annals*, 61(2):747–770, 2012.

[10] F. Bernachy-Barbé, L. Gélébart, L. Bornert, J. Crépin, and C. Sauder. Characterization of sic/sic composites damage mechanisms using digital image correlation at the tow scale. *Composites Part A: Applied Science and Manufacturing*, 68:101–109, 2015.

[11] J. Braun, C. Sauder, J. Lamon, and F. Balbaud-Célérier. Influence of an original manufacturing process on the properties and microstructure of sic/sic tubular composites. *Composites Part A: Applied Science and Manufacturing*, 123:170–179, 2019.

[12] Y. Chen, L. Gélébart, A. Marano, and J. Marrow. Fft phase-field model combined with cohesive composite voxels for fracture of composite materials with interfaces. *Computational Mechanics*, 68(2):433–457, 2021.

[13] X. Aubard and J. Lamon. Mechanical behaviour of 2 d-woven sic-sic composites under multiaxial loading conditions. In *High Temperature Ceramic Matrix Composites. Proc. 6 th European Conf. on Composite Materials*, volume 20, Bordeaux, France, 1993.

[14] HM. Yun, JA. DiCarlo, and DS. Fox. Issues on fabrication and evaluation of sic/sic tubes with various fiber architectures. In *Fifth International Conference on High Temperature Ceramic Matrix Composites (HTCMC-5)*, number NASA/TM-2004-213335, 2004.

[15] O. Gavalda Diaz and D. Axinte. Towards understanding the cutting and fracture mechanism in ceramic matrix composites. *International Journal of Machine Tools and Manufacture*, 118:12–25, 2017.

[16] L. Zhang, C. Ren, C. Ji, Z. Wang, and G. Chen. Effect of fiber orientations on surface grinding process of unidirectional C/SiC composites. *Applied Surface Science*, 366:424–431, 2016.

[17] O. Gavalda Diaz, G. Luna, Z. Liao, and D. Axinte. The new challenges of machining ceramic matrix composites (CMCs): Review of surface integrity. *International Journal of Machine Tools and Manufacture*, 139:24–36, 2019.

[18] A. Rösiger and R. Goller. Damage evaluation of CMCs after drilling with geometrically defined cutting edges. In *Materials Science Forum*, volume 825, pages 271–278. Trans Tech Publ, 2015.

[19] J. Chen, W. Ming, Q. An, and M. Chen. Mechanism and feasibility of ultrasonic-assisted milling to improve the machined surface quality of 2d cf/sic composites. *Ceramics International*, 46(10):15122–15136, 2020.

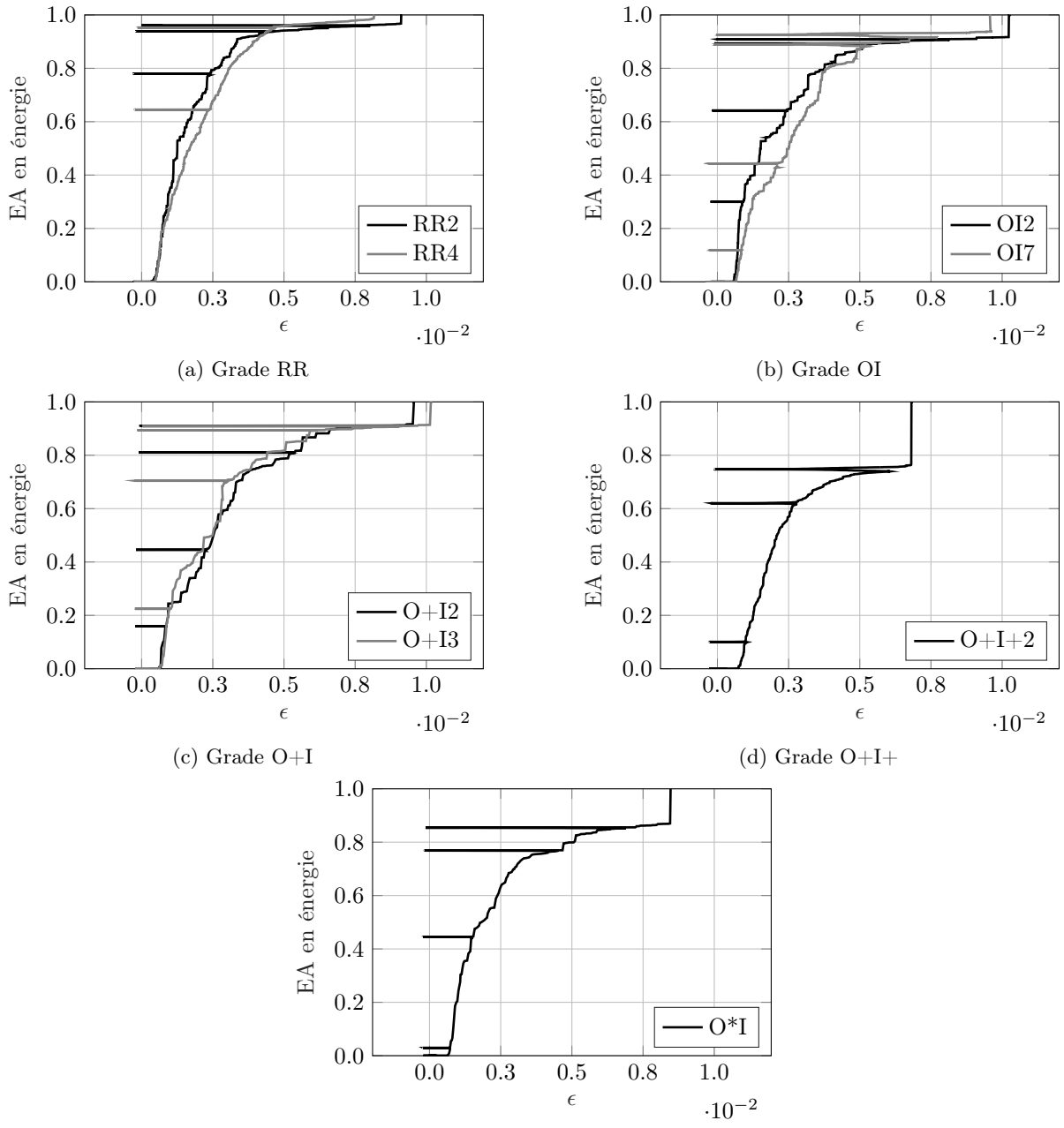


(a) Grade RR

(b) Grade OI

(c) Grade O+I

(d) Grade O+I+

(e) Grade O*I

Figure 27: Acoustic emission for some samples of five grades.

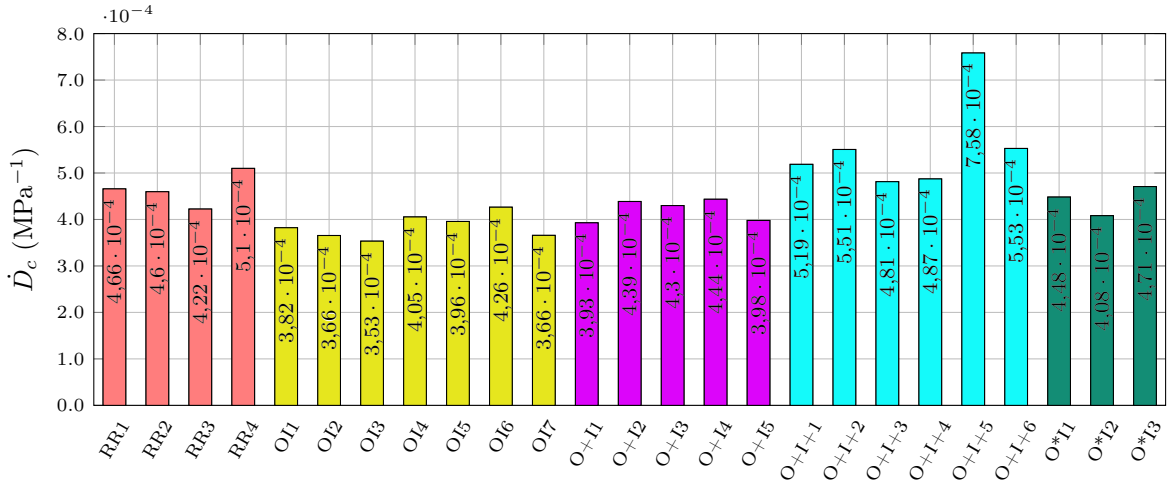


Figure 28: Shear damage speed $\dot{D}_c$ for the different samples.

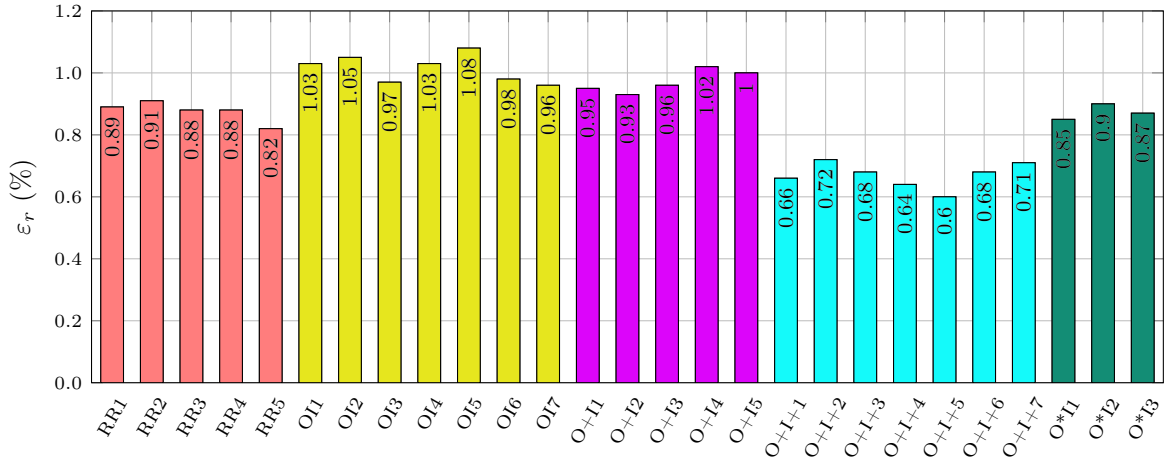


Figure 29: Strain at failure $\varepsilon_r$ for the different samples.

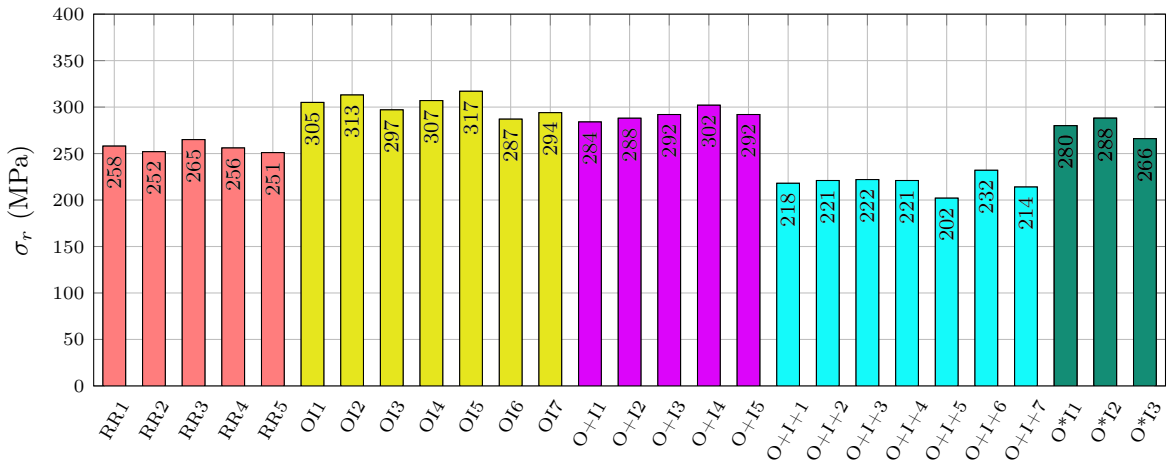


Figure 30: Stress at failure $\sigma_r$ for the different samples.

[20] X. Zhang, I. Yu, and J. Zhao. An analytical approach on stochastic model for cutting force prediction in milling ceramic matrix composites. *International Journal of Mechanical Sciences*, 168:105314, 2020.

[21] A. Rösiger, R. Goller, N. Langhof, and W. Krenkel. Influence of in-plane and out-of-plane machining on the surface topography, the removal mechanism and the flexural strength of 2d c/c-sic composites. *Journal of the European Ceramic Society*, 41(5):3108–3119, 2021.

[22] Y. Li, X. Ge, H. Wang, Y. Hu, E. Ning, W. Cong, and C. Ren. Study of material removal mechanisms in grinding of c/sic composites via single-abrasive scratch tests. *Ceramics International*, 45(4):4729–4738, 2019.

[23] Q. Liu, G. Huang, X. Xu, C. Fang, and C. Cui. A study on the surface grinding of 2D C/SiC composites. *International Journal of Advanced Manufacturing Technology*, 93(5-8):1595–1603, 2017.

[24] Q. Liu, G. Huang, X. Xu, C. Fang, and C. Cui. Influence of grinding fiber angles on grinding of the 2d–cf/c–sic composites. *Ceramics International*, 44(11):12774–12782, 2018.

[25] T. Tawakoli and B. Azarhoushang. Intermittent grinding of ceramic matrix composites (CMCs) utilizing a developed segmented wheel. *International Journal of Machine Tools and Manufacture*, 51(2):112–119, 2011.

[26] B. Azarhoushang. Wear of non-segmented and segmented diamond wheels in high-speed deep grinding of carbon fibre-reinforced ceramics. *The International Journal of Advanced Manufacturing Technology*, 74(9):1293–1302, 2014.

[27] T. Atkins. *The science and engineering of cutting: the mechanics and processes of separating, scratching and puncturing biomaterials, metals and non-metals*. Butterworth-Heinemann, 2009.

[28] A. Neubrand, J.M. Hausherr, A. Lauer, R. Weiss, and C. Wilhelmi. Investigation of cutting-induced damage in CMC bend bars. *MATEC Web of Conferences*, 29:1–12, 2015.

[29] N Lissart and J Lamon. Damage and failure in ceramic matrix minicomposites: experimental study and model. *Acta Materialia*, 45(3):1025–1044, 1997.

[30] J.-M. Domergue, E. Vagaggini, and A. Evans. Relationships between hysteresis measurements and the constituent properties of ceramic matrix composites: Ii, experimental studies on unidirectional materials. *Journal of the American Ceramic Society*, 78(10):2721–2731, 1995.

[31] E. Vagaggini, J-M. Domergue, and A. Evans. Relationships between hysteresis measurements and the constituent properties of ceramic matrix composites: I, theory. *Journal of the American Ceramic Society*, 78(10):2709–2720, 1995.

[32] C. Chateau, L. Gélébart, M. Bornert, J. Crépin, D. Caldemaison, and C. Sauder. Modeling of damage in unidirectional ceramic matrix composites and multi-scale experimental validation on third generation sic/sic minicomposites. *Journal of the Mechanics and Physics of Solids*, 63:298–319, 2014.

[33] J-W. Hutchinson and H-M. Jensen. Models of fiber debonding and pullout in brittle composites with friction. *Mechanics of materials*, 9(2):139–163, 1990.

[34] A-G. Evans and F-W. Zok. The physics and mechanics of fibre-reinforced brittle matrix composites. *Journal of Materials science*, 29(15):3857–3896, 1994.

[35] C. Morel, E. Baranger, J. Lamon, J. Braun, and C. Lorrette. The influence of internal defects on the mechanical behavior of filament wound sic/sic composite tubes under uniaxial tension. *Journal of the European Ceramic Society*, 2022.

[36] E. Buet, C. Sauder, D. Sornin, S. Poissonnet, J-N. Rouzaud, and C. Vix-Guterl. Influence of surface fibre properties and textural organization of a pyrocarbon interphase on the interfacial shear stress of SiC/SiC minicomposites reinforced with Hi-Nicalon S and Tyranno SA3 fibres. *Journal of the European Ceramic Society*, 34(2):179–188, feb 2014.

[37] C. Lorrette, D. Nunes, and C. Sauder. Patent EP2794515a1 (CEA): Process for fabrication of a part with tubular geometry made from a ceramic matrix composite material, 2016. US Patent 9,236,151.

[38] ISO. 121920-2:2021 - Spécification géométrique des produits (GPS) — État de surface: Méthode du profil — Partie 2: Termes, définitions et paramètres d'état de surface. Standard, International Organization for Standardization, 2021.

[39] ISO. 20323:2021 - Fine ceramics (advanced ceramics, advanced technical ceramics) – Mechanical properties of ceramic composites at ambient temperature in air atmospheric pressure – Determination of tensile properties of tubes. Standard, International Organization for Standardization, 2021.

[40] V. Pensée, D. Kondo, and L. Dormieux. Micromechanical analysis of anisotropic damage in brittle materials. *Journal of Engineering Mechanics*, 128(8):889–897, 2002.

[41] O. Gavalda Diaz, A. Axinte, P. Butler-Smith, and D. Novovic. On understanding the microstructure of sic/sic ceramic matrix composites (CMCs) after a material removal process. *Materials Science and Engineering: A*, 743:1–11, 2019.

[42] L. Li, X. Guo, and Y. Liu. Characterization of cyclic loading/unloading damage behavior in fiber-reinforced ceramic-matrix composites using inverse tangent modulus. *Journal of the European Ceramic Society*, 42(5):1912–1927, 2022.

[43] J. Aveston and A. Kelly. Theory of multiple fracture of fibrous composites. *Journal of Materials Science*, 8(3):352–362, 1973.

[44] J. Lemaitre, J-L. Chaboche, A. Benallal, and R. Desmorat. *Mécanique des matériaux solides-3e éd.* Dunod, 2020.